

INFORMATION TO USERS

This manuscript has been reproduced from the microfilm master. UMI films the text directly from the original or copy submitted. Thus, some thesis and dissertation copies are in typewriter face, while others may be from any type of computer printer.

The quality of this reproduction is dependent upon the quality of the copy submitted. Broken or indistinct print, colored or poor quality illustrations and photographs, print bleedthrough, substandard margins, and improper alignment can adversely affect reproduction.

In the unlikely event that the author did not send UMI a complete manuscript and there are missing pages, these will be noted. Also, if unauthorized copyright material had to be removed, a note will indicate the deletion.

Oversize materials (e.g., maps, drawings, charts) are reproduced by sectioning the original, beginning at the upper left-hand corner and continuing from left to right in equal sections with small overlaps. Each original is also photographed in one exposure and is included in reduced form at the back of the book.

Photographs included in the original manuscript have been reproduced xerographically in this copy. Higher quality 6" x 9" black and white photographic prints are available for any photographs or illustrations appearing in this copy for an additional charge. Contact UMI directly to order.

UMI

A Bell & Howell Information Company
300 North Zeeb Road, Ann Arbor MI 48106-1346 USA
313/761-4700 800/521-0600

MODELING AND SIMULATION OF A DIGITAL FOCUSING
SERVO CONTROL SYSTEM FOR AN OPTICAL
DISK TESTER

by
Farah Bates

A Thesis Submitted to the Faculty of the
DEPARTMENT OF ELECTRICAL AND COMPUTER ENGINEERING
In Partial Fulfillment of the Requirements
For the Degree of
MASTER OF SCIENCE
In the Graduate College
THE UNIVERSITY OF ARIZONA

1997

UMI Number: 1384553

UMI Microform 1384553
Copyright 1997, by UMI Company. All rights reserved.

**This microform edition is protected against unauthorized
copying under Title 17, United States Code.**

UMI
300 North Zeeb Road
Ann Arbor, MI 48103

STATEMENT BY AUTHOR

This thesis has been submitted in partial fulfillment of requirements for an advanced degree at The University of Arizona and is deposited in the University Library to be made available to borrowers under rules of the library.

Brief quotations from this thesis are allowable without special permission, provided that accurate acknowledgment of source is made. Requests for permission for extended quotation from or reproduction of this manuscript in whole or in part may be granted by the head of the major department or the Dean of the Graduate Collage when in his or her judgment the proposed use of the material is in the interests of scholarship. In all other instances, however, permission must be obtained from the author.

SIGNED: *Janah Bates*

APPROVAL BY THESIS DIRECTOR

This thesis has been approved on the date shown below:

F. E. Cellier

F. E. Cellier

Associate Professor of
Electrical and Computer Engineering

March 18, 1997

Date

ACKNOWLEDGMENTS

I wish to express my great appreciation to my thesis advisor Dr. Francois E. Cellier for his support, help, and encouragement. I am also very grateful to my committee members, Dr. Hal S. Tharp and Dr. Masud Mansuripur for their constructive review of this thesis.

I also wish to acknowledge my sincere gratitude to Tetsuo Semba and my husband, Keith Bates, for their invaluable guidance and discussions that helped me to go forward with this thesis.

I deeply appreciate my parents encouragement and support in my pursuit of knowledge.

TABLE OF CONTENTS

LIST OF ILLUSTRATIONS.....	5
LIST OF TABLES.....	7
ABSTRACT.....	8
1. INTRODUCTION.....	9
1.1 Optical Disk Tester.....	10
1.2 Background.....	12
1.3 Goal.....	14
1.4 Thesis Summary.....	17
2. SERVO LOOP MODEL.....	19
2.1 Focus Actuator Transfer Function.....	20
2.2 Focus Misregistration (FMR) Budget Specifications.....	24
2.3 Focus Servo Design.....	29
2.4 External Shock and Vibration.....	44
2.5 Shock and Vibration Requirements.....	46
2.6 Summary.....	59
3. DIGITAL CONTROLLER DEVELOPMENT.....	60
3.1 Issues of Importance in Digital Controller Implementation.....	60
3.1.1 Sample Rate Selection.....	61
3.1.2 Determination of the Anti-Aliasing Filter.....	63
3.1.3 A/D and D/A Converters.....	65
3.1.4 Addressing Computation Time Delay.....	68
3.1.5 Scaling the Control Law Variables.....	70
3.2 Discrete Models of the Controller and the Actuator.....	71
3.2.1 Discrete Models of the Compensator and Integrator.....	72
3.2.2 Discrete Model of the Actuator.....	84
3.2.3 Digital Modeling of the Whole Focus Servo System.....	92
3.3 Transient and Steady State Response Analysis.....	98
3.3.1 Transient Response and Steady State Error.....	99
3.4 Summary.....	104
4. Summary.....	106
4.1 Future Work.....	108
REFERENCES.....	110

LIST OF ILLUSTRATIONS

Fig. 1.1 Optical disk tester	12
Fig. 1.2 Focusing servo block diagram	17
Fig. 2.1 Mechanical free body diagram of the actuator	23
Fig. 2.2 Bode plots of the actuator	24
Fig. 2.3 Servo disturbances	28
Fig. 2.4 Bode plots of the lead compensator	37
Fig. 2.5 Bode plots of the practical integrator	39
Fig. 2.6 Bode plots of the compensated open loop transfer function	41
Fig. 2.7 Bode plots of the compensated closed-loop transfer function.....	42
Fig. 2.8 Bode plots of the error rejection	44
Fig. 2.9 External shock and vibration profile [6].....	46
Fig. 2.10 Mechanical free body of the shock mount	48
Fig. 2.11 Magnitude Bode plot of the shock mount	49
Fig. 2.12 Mechanical free body of the shock mount and the actuator	51
Fig. 2.13 Magnitude Bode plot of the response of the actuator and relative displacement of the lens for the shock and vibration.....	53
Fig. 2.14 Magnitude Bode plot of actuator and shock mount	54
Fig. 2.15 Bode plot of the accelerated error rejection	56
Fig. 2.16 Power density spectrum for closed-loop system.....	58
Fig. 3.1 Bode plots of the anti-aliasing filter	65
Fig. 3.2 Bode plots of the zero-order hold	68
Fig. 3.3 Computation delay phase for a sampling rate of 100 kHz	70
Fig. 3.4 Block diagram of the lead compensator	75
Fig. 3.5 Magnitude Bode plot of the compensator	76
Fig. 3.6 Phase Bode plot of the compensator.....	77
Fig. 3.7 Block diagram of the integrator	78
Fig. 3.8 Magnitude Bode plot of the integrator	80
Fig. 3.9 Phase Bode plot of the integrator.....	81
Fig. 3.10 Magnitude Bode plot of the compensator and integrator	83
Fig. 3.11 Phase Bode plot of the compensator and integrator.....	83
Fig. 3.12 Magnitude Bode plot of the actuator including the zero-order hold and the computation delay.....	91

Fig. 3.13 Phase Bode plot of the actuator including the zero-order hold and the computation delay	92
Fig. 3.14 Magnitude Bode plot of the complete open loop transfer function	94
Fig. 3.15 Phase Bode plot of the complete open loop transfer function	95
Fig. 3.16 Magnitude Bode plot of the closed loop transfer function	96
Fig. 3.17 Phase Bode plot of the complete closed-loop transfer function	97
Fig. 3.18 Unit step, transient response and steady state error	101
Fig. 3.19 Transient response and error to the sweeping sine wave	104

LIST OF TABLES

Table 2.1 Actuator parameters list	22
Table 2.2 FMR specifications	27
Table 2.3 Disk runout specifications	29
Table 2.4 Design target specifications for the analog servo system.....	35
Table 3.1 Anti-aliasing filter	64
Table 3.2 Compensator parameters	74
Table 3.3 Integrator parameters	80
Table 3.4 Difference equation coefficients	100
Table 3.5 Design target specifications for the digital servo control system	103

ABSTRACT

The design of a digital focus servo control system for an optical disk tester is presented. A total focus misregistration budget is established for three primary disturbances: disk runout, shock, and system noise. The design of an analog servo system is established first to determine the required bandwidth.

The analog design is transformed into a digital representation using pole/zero mapping techniques. The transformation to the digital domain includes the effects of the control law computation time, the D/A sample and hold, and the anti-aliasing filter.

Modeling and simulation of the digital system in the frequency and time domain are used to obtain the phase margin and the transient response. The transient response overshoot is larger than that obtained from a second order model. The larger overshoot is a result of the additional phase delay produced in the digital system that reduces the gain margin drastically compared to the analog case.

CHAPTER 1

1. INTRODUCTION

Optical data storage is currently in widespread use throughout the data processing industry to reliably store and retrieve large amounts of data. The data storage density using optical technology is increasing at a rate of an approximate double in capacity every two years. Shorter wavelength laser sources, improvements in optical media, and improvements in drive performance are some of the factors contributing to the increasing data storage density.

Current research in optical data storage requires the use of optical media testers to characterize new optical media in the early prototype stage. Many types of optical media are presently competing for this growing data storage market. Recently research efforts have produced an optical disk tester that

operates with many of these types of optical media. Presently this tester is using an analog servo system to maintain focus and tracking servo control. A digital control system could be used in this tester to greatly improve the performance of the tester. In Sections 1.2 and 1.3 we describe the potential performance improvements we expect to obtain by using a digital control system. In this report we describe the development of a digital servo control system to control the focusing of the laser beam produced by the optical media tester.

1.1 Optical Disk Tester

A schematic diagram of the optical disk tester is shown in Fig. 1.1. The optical disk tester is composed of the following principal components [1] :

- (i) An air- bearing spindle, which rotates in the range of 0 to 12000 rpm and holds the media.
- (ii) An objective lens is used to focus the laser light onto the optical disk.

- (iii) A relay lens system, which consist of optical elements that are adapted to a range of optical media thickness and operating wavelength. An aspheric singlet is mounted in the focus/tracking actuator, and is capable of motion along the optical axis (for focus adjustment) and along the radial direction of the disk (for track adjustment).
- (iv) A servo detector, which consists of an optical read out system for the light reflected by the disk to the detection unit (photo diodes).
- (v) A servo control system, which consist of the electronic circuits that enable the control of focusing and tracking operations.
- (vi) An actuator, which is an electromechanical device that converts the control command (current) for focusing and tracking into lens and spot displacement, respectively [2].

The objective for this study is the focus servo control system. In this document we only discuss the control of the lens motion along the optical axis of the actuator mechanism for the focusing operation. The focused spot must be driven by at least two position controls, namely one in the vertical (for focusing) and one in the radial (for tracking) direction, in such a way that the

track is followed accurately. These controls are usually called focus and tracking controls, respectively. The overall control functions are to maintain the laser in proper focus, to provide tracking on a desired groove on the rotating disk and to move radially to address different tracks on the disk.

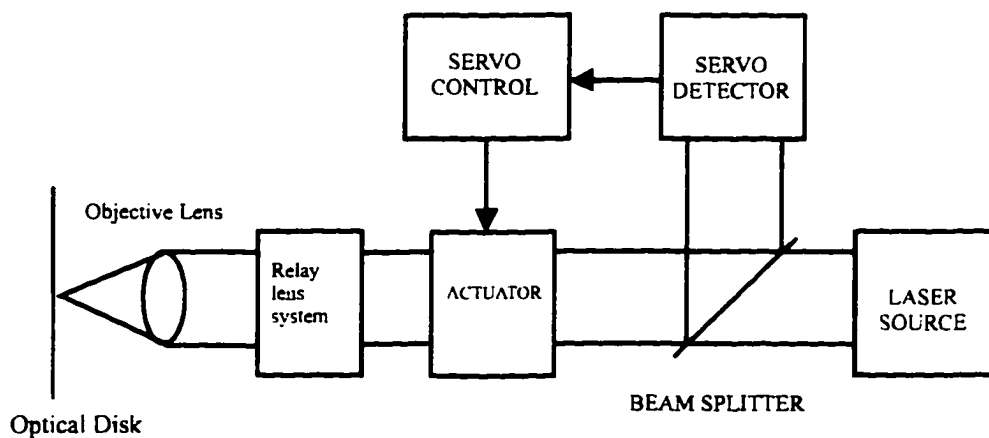


Fig. 1.1 Optical disk tester

1.2 Background

The optical tester operates with different laser wavelengths, media cover thickness layers, and media types (CDR, CDE, MO, WORM)*. In

* (CDR, compact disk recordable; CDE, compact disk erasable; MO, magneto optic; WORM, write once read many)

addition, the tester is versatile enough such that different optical schemes used to generate the focus and tracking error signals can easily be installed on the tester.

An analog servo system is not well adapted to this tester environment. Every time a change in the operation of the tester is made (media change, etc.) a lengthy calibration procedure must be performed by the operator to ensure proper operation of the servo system. The requirement to operate with different media types also brings mechanical resonance problems associated with particular media structures. The servo system in use must adapt to the changing media types to maximize system performance. Also, external shock and structural vibrations excite resonant behavior that can lead to an unstable servo system. A shock represents a sudden application of a force which results in a transient response of the tester. The shock force is an external disturbance to the actuator. Similarly, in the design of the focus servo, the performance criterion that is the most important is how well the system maintains the laser spot focused on the spinning optical disk that has a finite amount of axial runout. The axial runout of the disk (x_{disk}) is also a disturbance for the focusing servo.

1.3 Goal

A digital control system using a digital signal processor (DSP) for real time control of the focus and tracking servo loops will permit improved operation of the optical disk dynamic test system. Our goal is to replace the existing analog focus servo controller for the optical disk tester with a digital controller. The proposed block diagram of a digital servo control system for focusing is shown in Fig. 1.2. The forward control path in Fig. 1.2 consists of the following components:

- i. A DSP that implements the controller that is composed of a lead compensator and an integrator. The input to the DSP is the error signal $e(k)$.
- ii. A digital to analog converter (DAC) that converts the digital signal from the DSP into an analog signal. The DAC is modeled as a zero-order hold.
- iii. A power amplifier (PA) that provides the required current to drive the focus actuator.

- iv. K_{fa} is the gain constant of the actuator that converts the current through its coil to a force that moves the lens that is attached to the focus actuator.
- v. F_{vib} represents the shock and vibration force applied to the actuator as a disturbance.
- vi. The focus actuator is an electromechanical device that converts current to mechanical motion. A lens that focuses the laser light onto the optical disk is displaced by the mechanical motion of the actuator.
- vii. x_{lens} represents the dynamic position of the lens that focuses the laser light onto the optical disk.
- viii. x_{disk} represents the dynamic movement (runout) of the optical disk in the focus direction.

The feedback path consist of the following components:

- i. A focusing sensor that uses a portion of the light reflected from the media surface and generates a signal proportional to the focus error.
- ii. An anti-aliasing filter that removes unwanted signals generated by the focusing sensor.
- iii. An analog to digital converter (ADC) that converts the analog error signal into a discrete signal.

The programmability and flexibility of the digital control system permits the execution of repeatable calibration routines to adjust the servo operation parameters. For example, it may be necessary to adjust the open loop gain or bandwidth for certain media types and optical system variations. For an analog servo, the operator would need to adjust a potentiometer to change the gain. Also the operator would need to inject a sweeping sine wave signal (signal generator) to the analog controller box as an input and examine the output or the transfer function on the signal analyzer until the desired bandwidth or gain is achieved. With the digital controller the gain adjustment routine can be programmed into the DSP. The system requires commands from an operator to enter a preprogrammed calibration procedure for a particular optical disk under test. However, when a calibration procedure begins, no intervention is required by the operator. This automatic calibration procedure will improve the operation of the tester as the test conditions under which it operates are changed. In this document we describe the design of a digital focus servo loop that can be used with the optical disk tester. We do not discuss the implementation of any automatic calibration procedures.

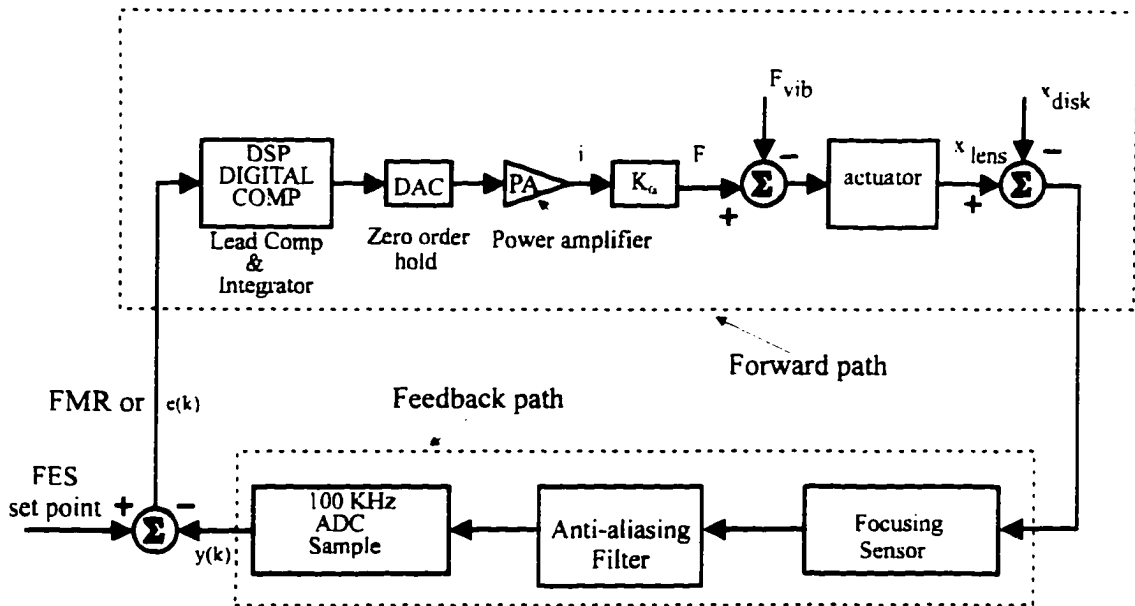


Fig. 1.2 Focusing servo block diagram

1.4 Thesis Summary

In Chapter 2, a model of the focus servo loop is described. The performance requirements of the focus servo loop are determined from the tester requirements. The focus control system must accommodate media runout displacements, and an operating shock and vibration environment. The transfer function of a commercially available focus actuator will be used to construct a model for the actuator. The system will first be modeled in the continuous time domain and then transformed to the digital domain.

In Chapter 3, the design compromises imposed by the digital transformation will be explored. The discrete models of the compensator and actuator will be determined. We will also study the digital simulation of the whole servo system in the frequency domain to determine the phase margin. Finally, we will look at the transient and steady state response of the servo system.

CHAPTER 2

2. SERVO LOOP MODEL

In this and succeeding chapters, we will discuss the design of the focus control servo. The models that will be used for the design of the controllers will be described. The design will be in the frequency domain and involves reshaping the Bode plots to meet the required specifications. Section 2.1 describes the model of a commercially available actuator. Section 2.2 contains the specifications for the focus misregistration budget. In Section 2.3, the servo bandwidth is determined based on the disk runout specification. In Section 2.4, we examine the servo performance in the presence of the appropriate shock and vibration disturbances.

2.1 Focus Actuator Transfer Function

A mechanical free body diagram illustrating the structure of the actuator is provided in Fig. 2.1. M_a represent the mass of the lens and moving parts inside the actuator, K_{sa} is the spring constant for the restoring force, and b_a is the viscous damping factor. The electromagnetic force F on the lens is produced by an electric current I through the coil. K_{fa} is the ratio of the force F on the actuator to the electric current (I). The equation of motion of the mass is,

$$M_a \ddot{y}(t) + b_a \dot{y}(t) + K_{sa} y(t) = K_{fa} I(t) \quad (2.1)$$

Using the Laplace transform we obtain the actuator transfer function in the frequency domain,

The transfer function of the actuator can be written in the form,

$$G_a(s) = \frac{y(s)}{I(s)} = \frac{\frac{K_{fa}}{M_a}}{s^2 + 2\zeta_a s \omega_{na} + \omega_{na}^2} \quad (2.2)$$

where ω_{na} is the resonant frequency, and ζ_a is the damping factor. The natural resonant frequency is,

$$\omega_{na} = \sqrt{\frac{K_{sa}}{M_a}} \quad (2.3)$$

where K_{sa} denotes the spring constant. The damping factor is,

$$\zeta_a = \frac{b_a}{2\sqrt{K_{sa}M_a}} \quad (2.4)$$

The values of the parameters for the actuator model are estimated from the measured response of the actuator of the existing analog controller. The measured actuator response was obtained by calculating the open-loop response from the measured closed loop response. The closed loop response was measured using the swept sine method and a dynamic spectrum analyzer. Because it was not practical to disassemble the actuator to measure the individual components, we estimated the actuator parameters using our best judgment, such that the measured response was the same as that given

by Eq. (2.2). The estimated parameters of the actuator model are given in Table 2.1.

Table 2.1 Actuator parameters list

DESCRIPTION	NOTATION	VALUE
Resonant frequency	ω_{na}	50 radian/sec
Damping factor	ζ_a	0.25
Spring constant	K_{sa}	50 newtons / meter
Lens mass	M_a	0.02 Kg
Viscous damping factor	b_a	0.5 newtons / meter / sec
Force constant	K_{fa}	1 newtons / amp

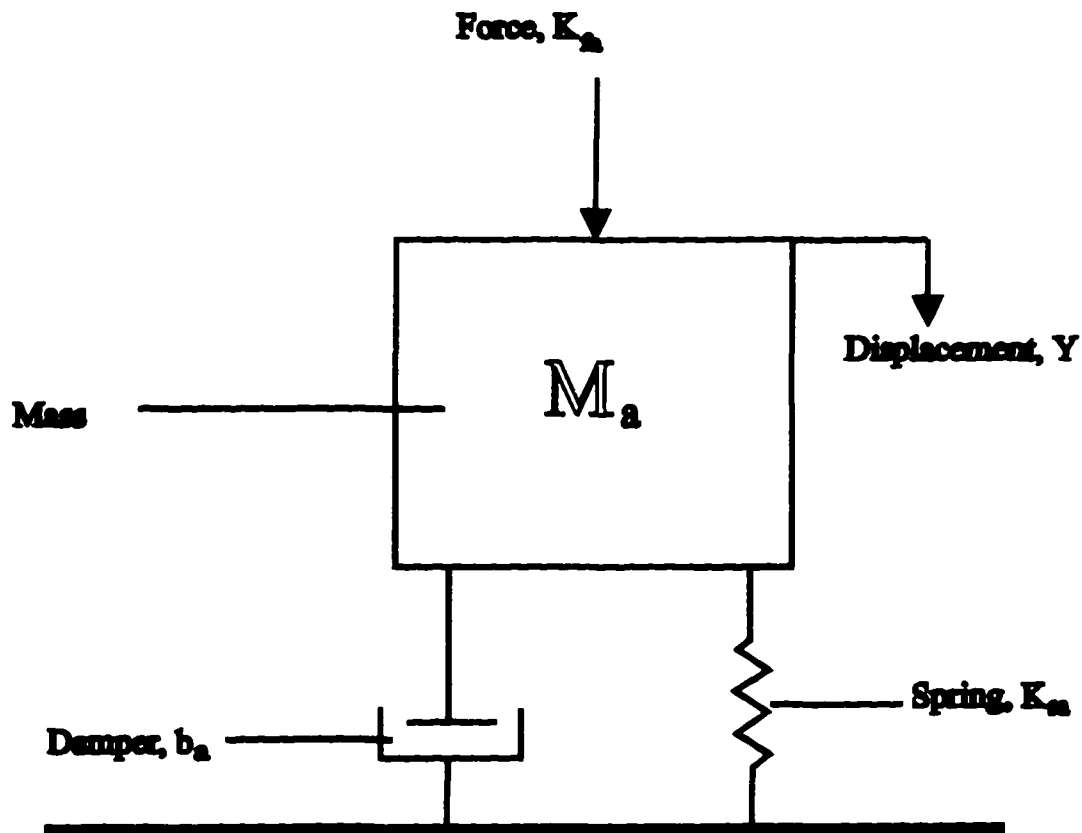


Fig. 2.1 Mechanical free body diagram of the actuator

The amplitude and phase Bode plots of the actuator transfer function are shown in Fig. 2.2. A resonance peak at 8 Hz is clearly shown. For modeling purposes, at low frequencies ($s \rightarrow 0$) the gain is normalized to one by multiplying the numerator of Eq. (2.2) with $M_a \cdot \omega_{na}^2$. For the real servo control system this constant gain difference will be added to the power

amplifier that drives the actuator. For frequencies greater than ω_{na} the transfer function is estimated as $1/s^2$, resulting in a negative slope of 40 dB decade and a phase of -180° . At the resonance frequency (ω_{na}), the phase is -90° as expected.

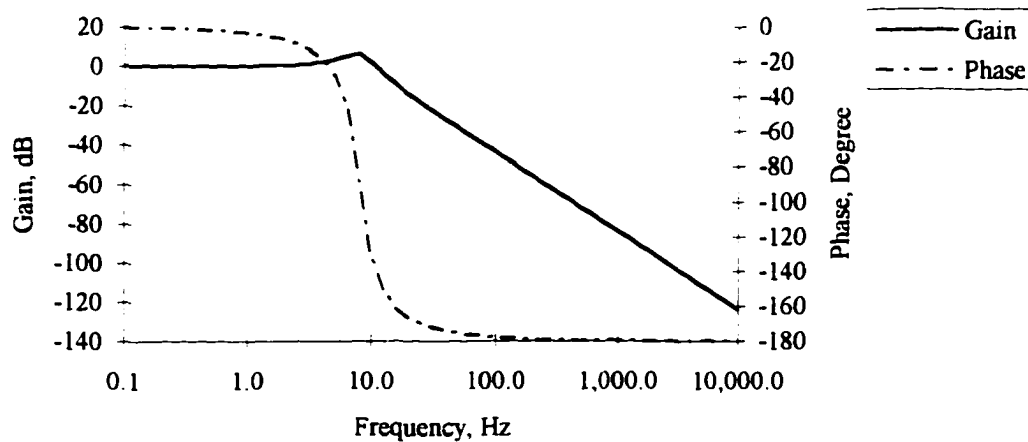


Fig. 2.2 Bode plots of the actuator

2.2 Focus Misregistration (FMR) Budget Specifications

In the design process for the optical disk tester each subsystem is allowed to have performance variations. An “error budget” is established for

each subsystem so that the total system's errors will allow the system to perform within its specifications.

During the closed loop operation of the focus servo loop, the difference between the output of the ADC and the focus error signal (FES) set point (see Fig. 1.2) is defined as focus misregistration (FMR). Ideally the FMR is zero. For the real system the FMR is divided up into individual random errors that are added to obtain a total FMR error budget. The total FMR error budget is determined by the allowable focus error that results in an acceptable spot size on the optical disk [3].

Focus misregistration (FMR) is the contribution of three primary sources of disturbances: disk lateral movement, shock and vibration, and system noise. The system noise and shock and vibration are random disturbances with means of zero and standard deviations of σ_s and σ_v , respectively. The disk runout is a periodic (sine wave) disturbance with a peak to peak value of $400 \mu\text{m}$ ($\pm 200\mu\text{m}$) and a mean value that is dependent upon the mechanical tolerance between the rest position of the lens and the disk surface. The optical disks are produced by a manufacturing process that

results in a range of disk runout with a Gaussian distribution and a 3σ value of $\pm 200\mu\text{m}$. These disturbances are all modeled as independent Gaussian distributions as shown in Fig. 2.3. During closed loop operation of the servo system, with a pure integration included in the compensator the total error will have a mean value approaching zero, and a 3σ value according to the system specification shown in Table 2.2. Now we can model the total variance, $(3\sigma_{\text{FMR}})^2$ as,

$$(3\sigma_{\text{FMR}})^2 = (3\sigma_d)^2 + (3\sigma_v)^2 + (3\sigma_s)^2 \quad (2.5)$$

This results in a probability density function (PDF) as shown in Fig. 2.3. The individual Gaussian distributions for the above disturbances and the FMR are identified in Fig. 2.3 and Table 2.2 with their 3σ values.

The $\pm 3\sigma_{\text{FMR}}$ corresponds to the probability of finding errors greater than 3σ which is 0.0026. The disk lateral movement produces periodically occurring disturbances into the servo system which can be modeled as a Gaussian distribution with mean power of σ_d^2 . The external shock and vibration are also modeled as a random noise disturbance and have Gaussian

distribution with mean power of σ_v^2 . The system noise is randomly distributed and has a Gaussian distribution with mean noise power of σ_s^2 .

The design of the focus servo is based on the following specifications:

The total error budget is modeled as a Gaussian distribution with a 3σ value of 0.5 microns ($3\sigma_{\text{FMR}}$) [4]. It is divided up as 0.1 microns for the system noise [4] (media noise, crosstalk, electronics noise, etc , that are all randomly distributed) and the remaining is divided up equally between the disk lateral movement and shock and vibrations (0.346 microns each) according to Eq. (2.5).

Table 2.2 FMR specifications

FOCUS MISREGISTRATION (FMR) SPECIFICATIONS		
DESCRIPTION	NOTATION	VALUE
Total FMR 3σ	$3\sigma_{\text{FMR}}$	0.5 μm
FMR 3σ for disk runout	$3\sigma_d$	0.346 μm
FMR 3σ for vibration	$3\sigma_v$	0.346 μm
FMR 3σ for system noise	$3\sigma_s$	0.1 μm

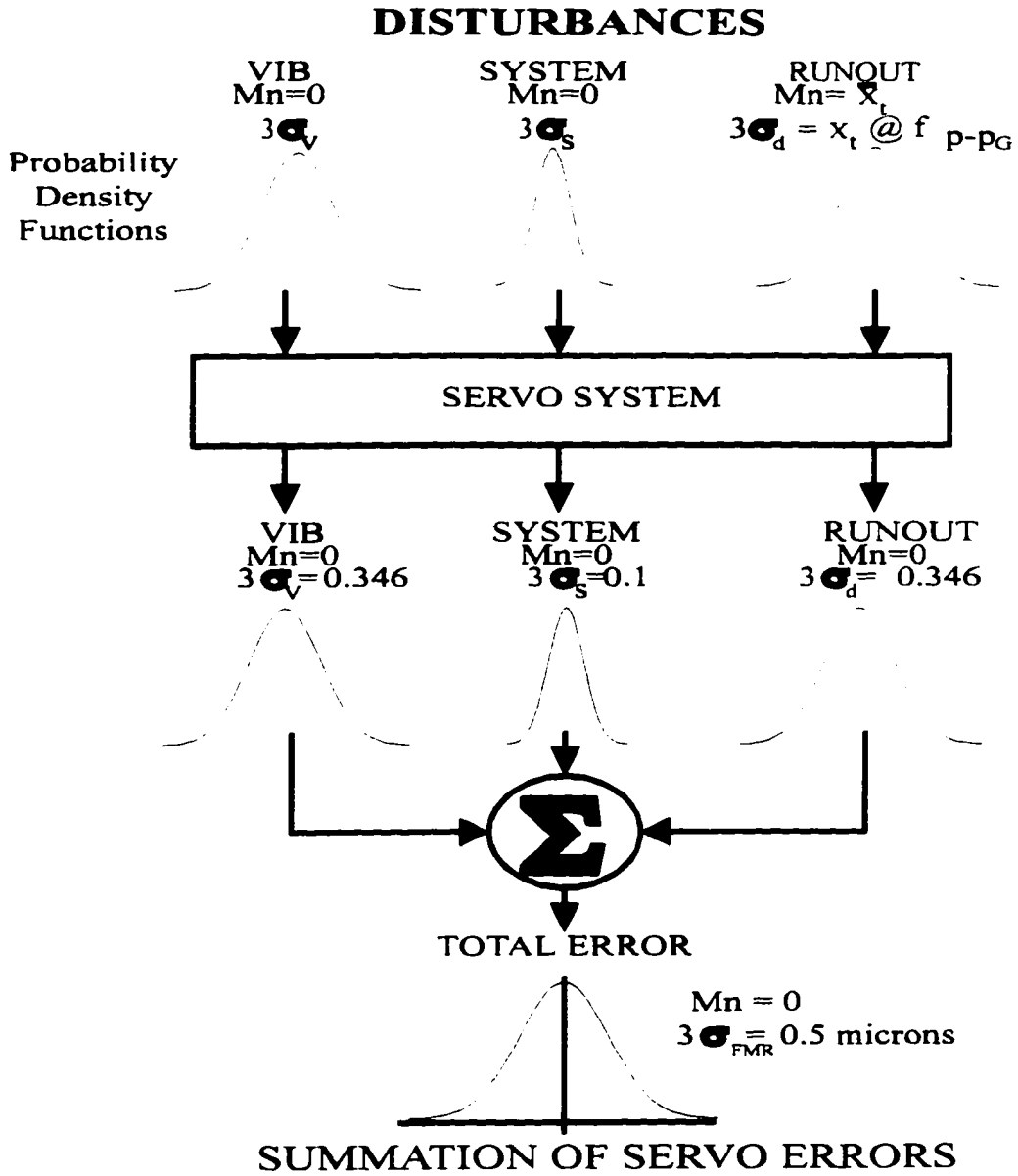


Fig. 2.3 Servo disturbances

2.3 Focus Servo Design

In this section we present a design of the focus servo loop to correct for the disturbance caused by lateral movement of the media during rotation. A determination of the focus servo bandwidth necessary to overcome the expected disturbance is described first.

The maximum disk rotation speed for our design is 3600 rpm which corresponds to a 60 Hz fundamental frequency. The uncorrected disk runout error at the fundamental frequency is 200 microns [4] and the corrected error is 0.346 microns as shown in Table 2.3.

Table 2.3 Disk runout specifications

DISK RUNOUT SPECIFICATIONS		
DESCRIPTION	NOTATION	VALUE
Uncorrected error	$E_{uc} @ f_1$	$\pm 200 \mu\text{m}$
Corrected error	$E_c @ f_1$	$0.346 \mu\text{m}$
Mechanical tolerance	Tol_m	$\pm 200 \mu\text{m}$
Disk rotation speed	f_1	60 Hz

To estimate the servo bandwidth, the amount of error rejection is first calculated. The error rejection is the ratio of the corrected error to the uncorrected error. For a closed loop servo with open loop transfer function $G_t(s)$ this ratio is given by [2],

$$\frac{E_c(s)}{E_{uc}(s)} = \frac{1}{1+G_t(s)}, \quad (2.6)$$

where E_c is the corrected error (the continuous time equivalent of $e(k)$ shown in Fig. 1.2). E_{uc} is the total disk runout (x_{disk} shown in Fig. 1.2), and $G_t(s)$ is the open loop gain of the servo system. The ratio of E_c and E_{uc} is called error rejection E_r [2],

$$E_r(s) = \frac{1}{1+G_t(s)}. \quad (2.7)$$

The $|E_r(s)|$ determines the amount of error reduction at any frequency. The error rejection $E_r(s)$, gives the fraction of the incoming disturbance (uncorrected error) which remains as a residual error (corrected error) after feedback.

The system gain of the focus servo G_t at the fundamental frequency f_1 (60Hz) can be derived from Eq. (2.6). The necessary open loop gain to obtain the desired error rejection is

$$G_{t1} = G_t(s) \Big|_{s=j2\pi f_1} = \frac{E_{uc}(j2\pi f_1)}{E_c(j2\pi f_1)} - 1, \quad (2.8)$$

where G_{t1} is the product of the focusing sensor, the lead compensator and integrator circuit response, and the actuator response at the fundamental frequency. By substituting the values for E_c and E_{uc} at fundamental frequency into Eq.(2.8), we obtain a value for G_{t1} of 55.2 dB.

The system gain at high frequencies is estimated to be proportional to $1/s^2$ ($s = j2\pi f$). $G_t(s)$ at the fundamental frequency, f_1 , and the crossover frequency, f_2 , is,

$$G_t(j2\pi f_1) \propto \frac{1}{f_1^2}, \quad (2.9)$$

$$G_t(j2\pi f_2) \propto \frac{1}{f_2^2}. \quad (2.10)$$

At the open loop crossover frequency f_2 , $G_t(j2\pi f_2)$ is equal to one. The ratio of Eq. (2.9) and Eq. (2.10) allows us to roughly estimate the crossover frequency f_2 as,

$$f_2 = f_1 \cdot \sqrt{G_t(j2\pi f_1)}. \quad (2.11)$$

Using a value of 60 Hz for f_1 and a $G_t(j2\pi f_1)$ of 577 (55.2 dB), we obtain $f_2 = 1441$ Hz.

The actual servo bandwidth is obtained by also considering the effect of the lead compensator. The compensator depresses the slope of $1/s^2$ of $G_t(s)$ to approximately $1/s$ around the f_2 region which causes the $1/s^2$ slope to be shifted to the left. If we consider f_2 obtained by Eq. (2.11) as the crossover frequency for the compensator, the whole Bode plot for the cascade combination of the actuator and the compensator will shift to the left and it will reduce the gain at the fundamental frequency. To compensate for this, the crossover frequency of the compensator is obtained by gradually increasing or shifting to the right by means of iterative calculation to achieve the target error rejection $E_r(s)$ at the fundamental frequency. The resulting crossover frequency is

$$f_c = 1.874 \cdot f_2 = 2700 \text{ Hz} \quad (2.12)$$

The compensator is inserted into the system in cascade to meet the design target specifications in Table 2.4. The transfer function for the compensator is

$$G_c(s) = K_c \frac{1 + \alpha T_c s}{1 + T_c s}, \quad (2.13)$$

where α is the ratio between the pole and the zero frequencies, T_c is the time constant and is obtained from the frequency at which the maximum phase lead occurs [5],

$$T_c = \frac{1}{2\pi f_c \sqrt{\alpha}}. \quad (2.14)$$

The phase lead at the crossover frequency is [5],

$$\phi_c = a \sin\left(\frac{\alpha - 1}{\alpha + 1}\right) \quad (2.15)$$

The lead compensator has gain G_{mc} at f_c . The value for G_{mc} is obtained by substituting T_c from Eq. (2.14) into the compensator transfer function and setting K_c and s equal to one and $2\pi f_c$, respectively. We have,

$$G_{mc} = \frac{1 + \sqrt{\alpha}}{1 + \frac{1}{\sqrt{\alpha}}} \quad (2.16)$$

Table 2.4 Design target specifications for the analog servo system.

FOCUS SERVO DESIGN TARGET		
DESCRIPTION	NOTATION	VALUE
Peaking	$T_{CL} @peaking$	1.7 dB
Overshoot	-	10%
Phase margin	θ_{10}	60°
Alpha	α	15
Resulting bandwidth	BW	2.7 kHz

The gain constant K_c is determined by the requirement for unity gain at f_c for the cascade combination of the actuator and compensator. To obtain unity gain for the cascade combination of the actuator and compensator, we need to divide the gain of the actuator at f_c by the gain of the compensator at f_c (G_{mc}). The gain of the actuator at f_c is obtained from Eq.(2.11). The gain constant K_c is,

$$K_c = \frac{\left(\frac{2\pi f_c}{\omega_{na}}\right)^2}{G_{mc}} \quad (2.17)$$

The amplitude and phase Bode plots for the lead compensator are shown in Fig. 2.4. Fig. 2.4 shows that the maximum phase of the compensator is located at the crossover frequency f_c as expected. The pole and zero separation, the gain constant G_{mc} , and the phase constant θ_c are dependent on the value of α . α is determined by the phase margin requirements of the design as shown in Table 2.4.

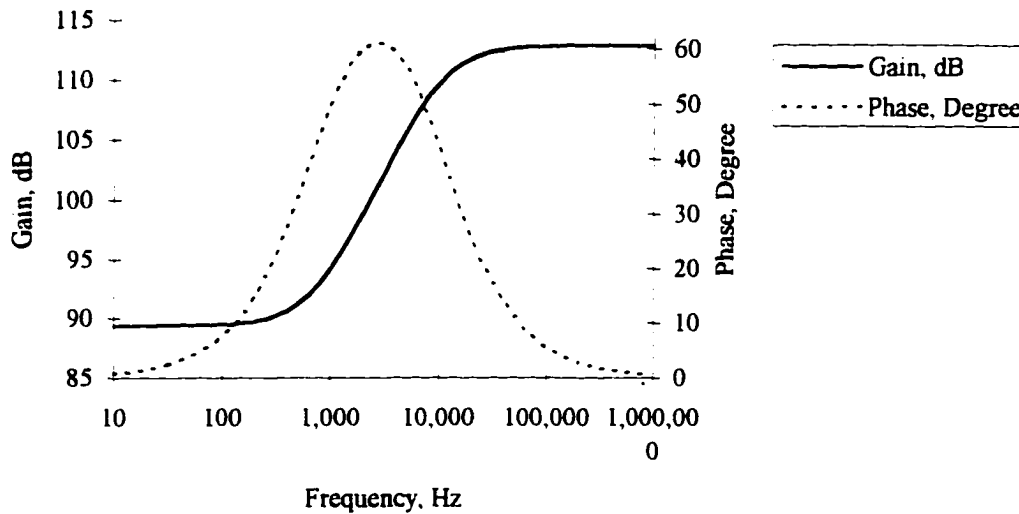


Fig. 2.4 Bode plots of the lead compensator

An integrator is necessary to reduce the steady state error. A practical integrator has a nonzero pole as opposed to the ideal integrator which has a single pole at the origin. Also the purpose of the integrator is to increase the gain at low frequencies resulting in improved error rejection at low frequencies. The frequency response of a real integrator is shown in Fig. 2.5. Note that the pole and zero frequencies of the practical integrator are 0.1 and 30 Hz, respectively. At low frequencies, the departure of the practical integrator from the ideal integrator is due to the nonzero pole. The ideal

integrator has its pole at zero frequency which will result in zero steady state error. The smaller the practical integrator's pole frequency, the smaller the resulting steady state error. At high frequencies the departure is due to the practical integrator's zero response at 30 Hz. The practical integrator's zero is selected at 30 Hz to minimize the reduction in the phase margin by the integrator. A phase margin loss of 0.6° results which provides the required phase margin of 60° for stability. If the integrator's zero becomes larger than 30 Hz, it will reduce the phase margin and the stability of the system.

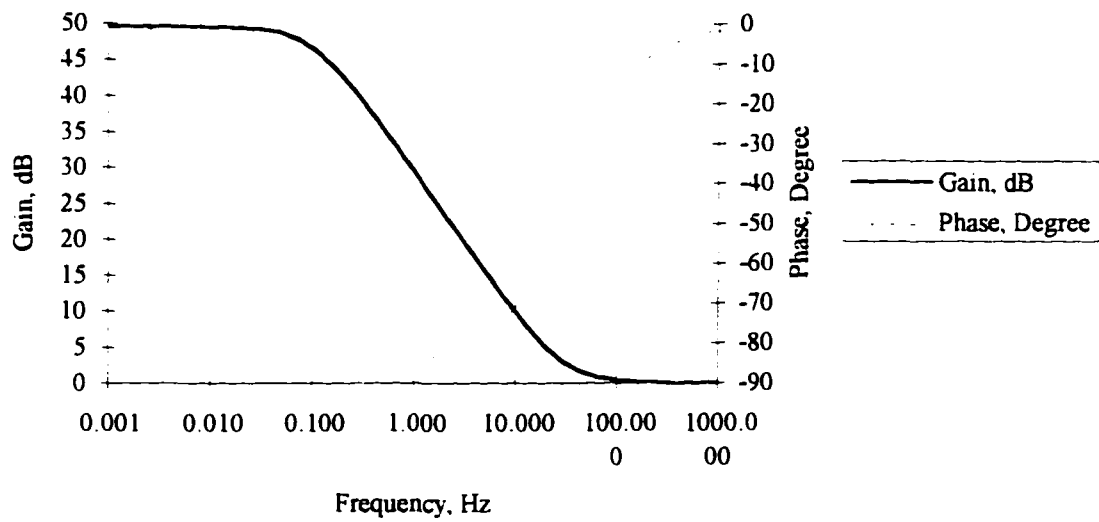


Fig. 2.5 Bode plots of the practical integrator

The transfer function of the practical integrator is,

$$G_i(s) = \frac{s + \omega_z}{s + \omega_p} \quad (2.18)$$

where ω_z , ω_p are the zero and pole frequency at 0.628 and 188.49 radian/sec, respectively.

The compensated open loop transfer function with the integrator for the analog system is,

$$G_{lo}(s) = G_c(s)G_a(s)G_i(s) \quad (2.19)$$

The Bode plot is shown in Fig. 2.6. Fig. 2.6 shows a maximum servo gain of approximately 138 dB at low frequencies. This maximum gain is effective for reducing steady state errors attendant to the mechanical precision and the stability of the drive and media tolerances. For example with a gain of 138 dB, if the mechanical tolerance, Tol_m , at the rest position is $\pm 200 \mu\text{m}$ (see Table 2.3), the focus error is $\pm 25 \cdot 10^{-6} \mu\text{m}$ during closed loop operation of the servo at low frequencies. The gain of 138 dB at low frequency produces a negligibly small steady state error of $\pm 25 \cdot 10^{-6} \mu\text{m}$.

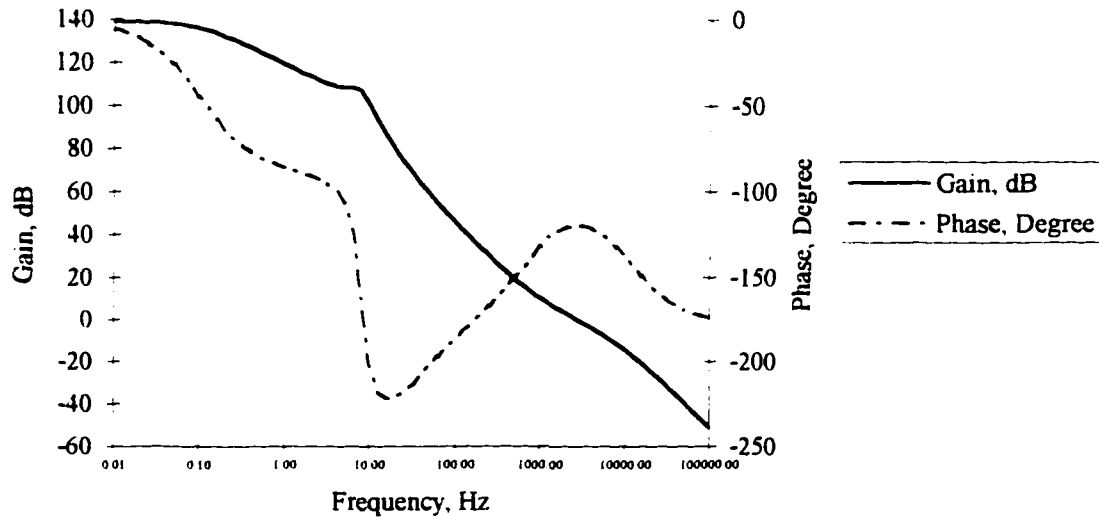


Fig. 2.6 Bode plots of the compensated open loop transfer function

The compensated closed loop transfer function is,

$$T_{cl} = \frac{G_{lo}(s)}{1 + G_{lo}(s)} \quad (2.20)$$

The Bode plot is shown in Fig. 2.7. Fig. 2.7 shows a gain of 0 dB up to 100 Hz and also at the crossover frequency (2700 Hz). The peaking between 1 kHz and 2.7 kHz is attendant to the phase margin produced by the lead

compensator. The peaking at 1.22 kHz is 1.7 dB. The peaking of the closed loop response is in agreement with our design target shown in Table 2.4.

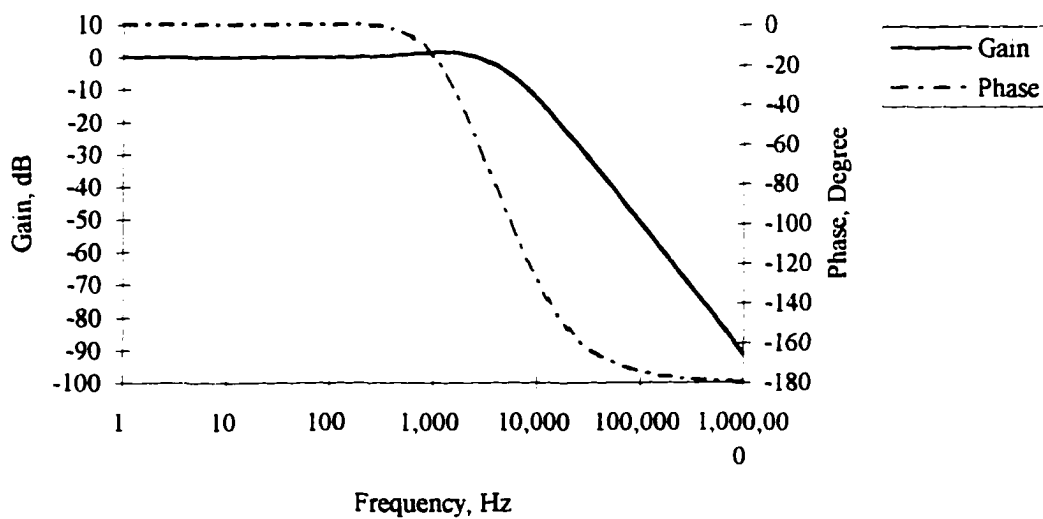


Fig. 2.7 Bode plots of the compensated closed-loop transfer function

The error rejection for the compensated system is equal to

$$T_e(s) = \frac{1}{1 + G_{to}(s)} \quad (2.21)$$

The amplitude and phase Bode plots for above equation are shown in Fig. 2.8. Fig. 2.8 shows a very good error rejection ($\approx 10^{-8}$) at very low frequencies (0 to .001 Hz). The error rejection ability reduces as the frequency increase until it reaches 0db at the crossover frequency. Any error at frequencies higher than the crossover frequency will not be corrected. The error rejection at the fundamental frequency is -55.49 dB. If the disk runout at the fundamental frequency is $\pm 200 \mu\text{m}$, the resulting focus error attendant to the disk runout is $\pm 0.336 \mu\text{m}$. This calculated focus error is approximately equal to the amount that we budgeted in Section 2.3 as shown in Table 2.3. We can conclude that the designed servo bandwidth (2700 Hz) is adequate to reject the disk runout during closed loop operation. In the next section, we will examine the effectiveness of the servo control system with this servo bandwidth of 2700 Hz to reject the errors due to shock and vibrations.

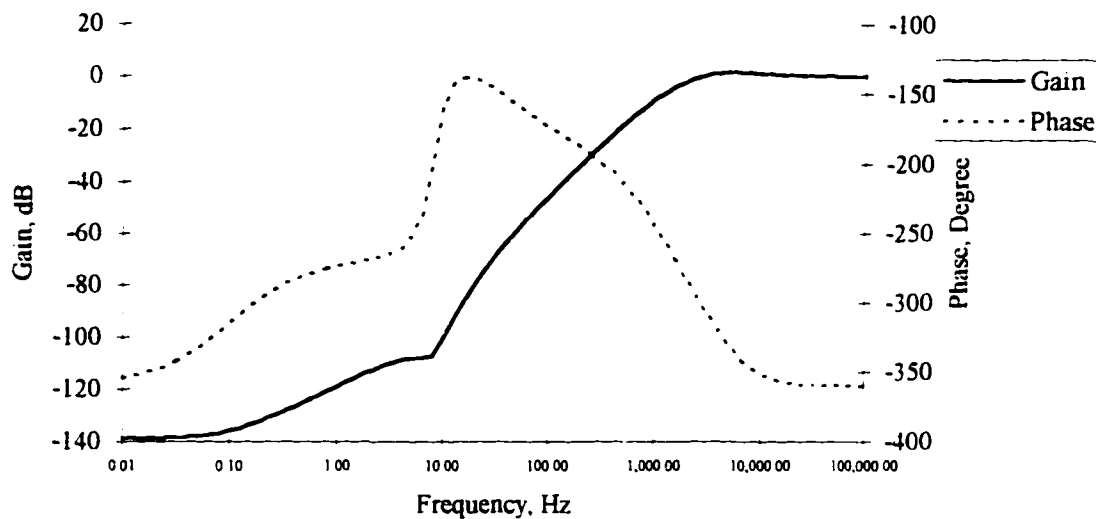


Fig. 2.8 Bode plots of the error rejection

2.4 External Shock and Vibration

The design of the focus servo is now examined based only on external shock and vibration excitation to the system independent of the media lateral displacement. The external shock and vibration is applied to the device through a range of frequencies from 5 to 500 Hz. The applied interpolated power density spectrum [6], Vib (G^2 per Hz) is shown in Fig. 2.9, where one

G (gravitational force) is equal to 9.8 meter per sec². The integration of the input power density spectrum over the frequency range of 5 to 500 Hz will result in a root mean square (RMS) of 0.67 Gs.

Our objective is to calculate the RMS value of the resulting displacement error. To accomplish this objective, first we need to model the shock mount and the actuator transfer function for shock and vibration. Next, with the input power density of the shock and vibration, the corrected displacement error can be calculated. The calculation of the resulting displacement error is presented in Section 2.5.

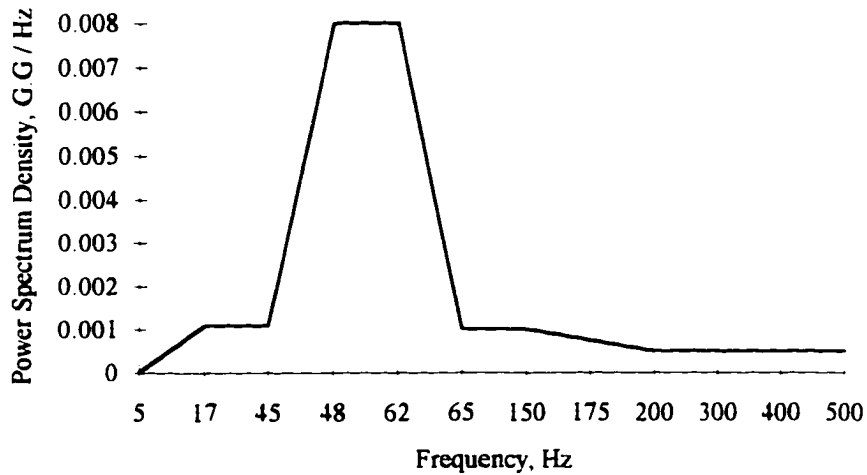


Fig. 2.9 External shock and vibration profile [6]

2.5 Shock and Vibration Requirements

The shock mount and actuator body assembly is modeled as a spring-mass-dashpot system as shown in Fig. 2.10. Notice that the force with displacement X_i is applied to the base of the spring-mass-dashpot, not to the mass M_a as shown in Fig. 2.1. This means that the force has to pass through the lead network of the spring and the damper. From inspection of Fig. 2.10, the transfer function representation of the shock mount model is

$$Shock(s, Q, \omega) = \frac{X_0(s)}{X_1(s)} = \frac{\frac{\omega}{Q}s + \omega^2}{s^2 + \frac{\omega}{Q}s + \omega^2}, \quad (2.22)$$

where Q is the quality factor ($Q = 1/2\zeta$). The Bode plot for the transfer function given by Eq. (2.22) is shown in Fig. 2.11, for a Q of 0.5 and a resonant frequency, ω , of 70.0 Hz [6].

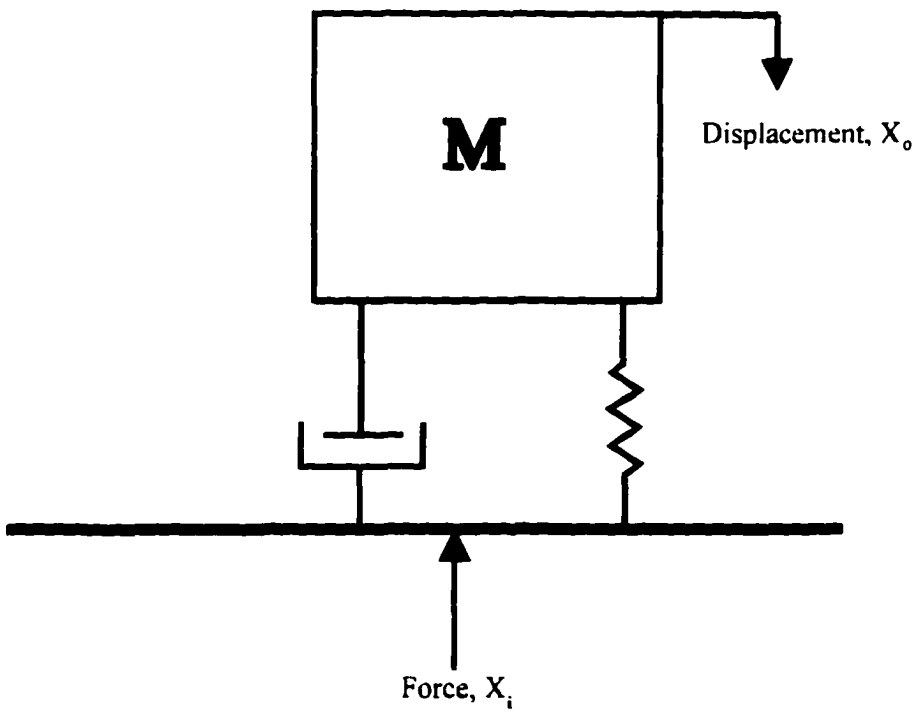


Fig. 2.10 Mechanical free body of the shock mount

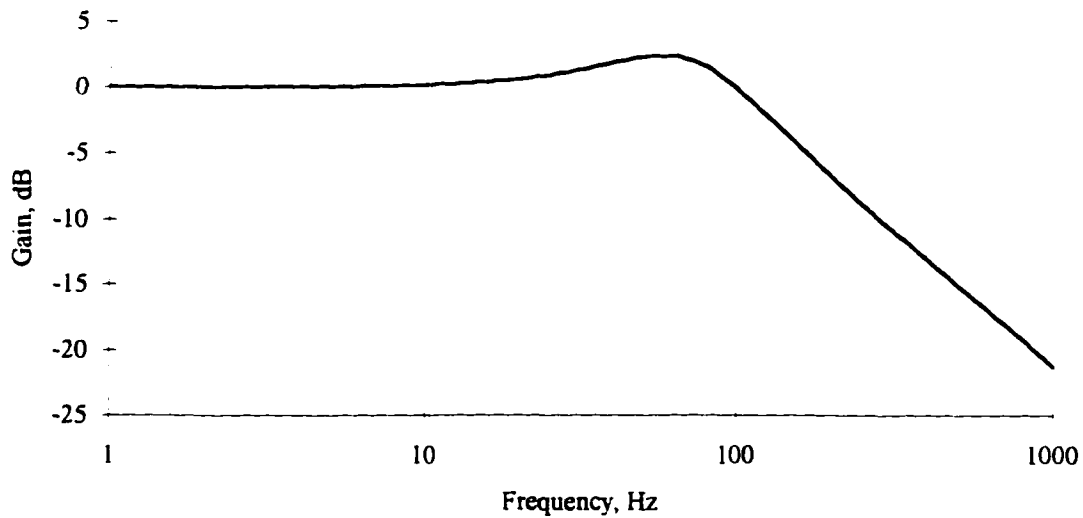


Fig. 2.11 Magnitude Bode plot of the shock mount

The shock mount transmits the external shock and vibration to the disk and actuator as shown in Fig. 2.12. In this report we modeled the body of the actuator and the disk as one rigid body as shown in Fig. 2.12. The lens and moving parts inside the actuator is the mass (M_L) shown in Fig. 2.12. Our objective is to find the relative displacement of the lens compared to the disk displacement when a force with displacement x_i is applied to the system through the shock mount. First, we know the displacement of the lens is equal to the displacement of the actuator body multiplied by the actuator transfer

function. The disk displacement is equal to the displacement of the actuator body, because the disk is modeled as a rigid body attached to the base as shown in Fig. 2.12. With these assumptions, the disk will move by the same amount as the actuator body. The relative displacement of the lens compared to the disk is,

$$x_0(s) = x_1(s)(1 - T_{actuator}(s)) \quad (2.23)$$

The resulting transfer function for relative displacement of the lens is

$$1 - T_{actuator}.$$

The transfer function of the lens relative to the disk, G_b , is,

$$G_b(s) = (1 - T_{actuator}(s)). \quad (2.24)$$

For the mechanical model of the actuator as shown in Fig. 2.10, the transfer function is,

$$T_{actuator}(s) = \frac{2\zeta_a \omega_{na} s + \omega_{na}^2}{s^2 + 2\zeta_a \omega_{na} s + \omega_{na}^2} \quad (2.25)$$

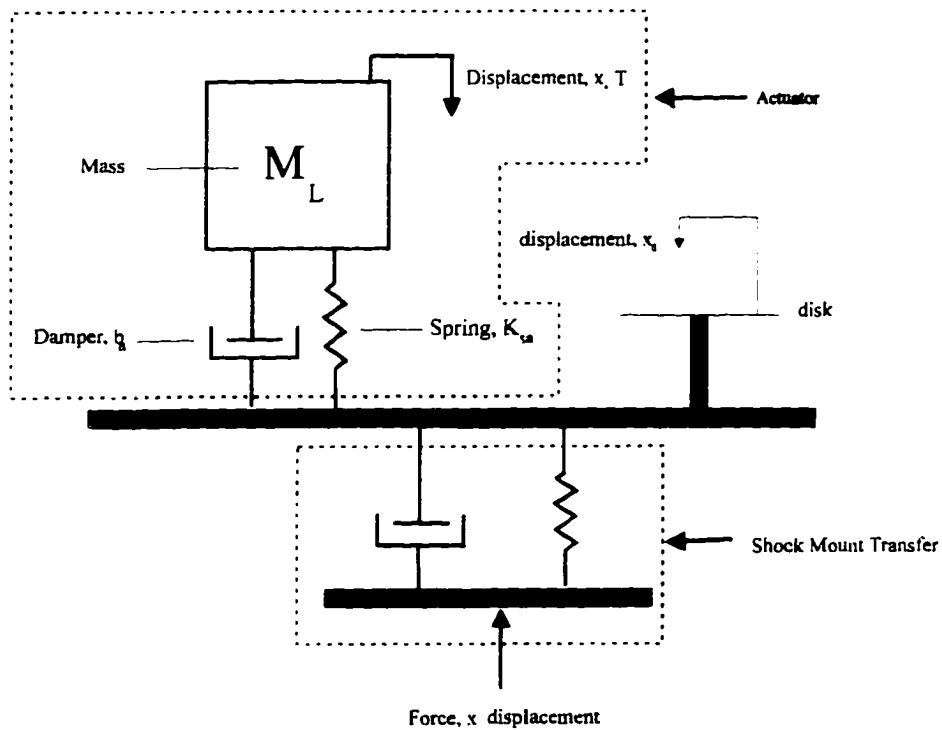


Fig. 2.12 Mechanical free body of the shock mount and the actuator

The amplitude Bode plot of the actuator transfer function given by Eq. (2.25) with resonant frequency, $\omega_{na}=8$ Hz and damping factor, $\zeta_a=0.25$ and the relative displacement of the lens transfer function for the shock and vibration are both shown in Fig. 2.13.

For the relative displacement transfer function at low frequencies, the gain increases as the frequency increases up to the resonant frequency. This is because for very low frequencies the lens moves with the base, and a very small displacement difference between the lens and the base results. As the frequency increases, the displacement difference increases because more force is required to move the lens. At resonance the displacement difference reaches its maximum value. At high frequencies the lens is almost stationary relative to the disk surface so the relative displacement approaches unity. The mean applied force for shock is constant (RMS value of 0.67 Gs).

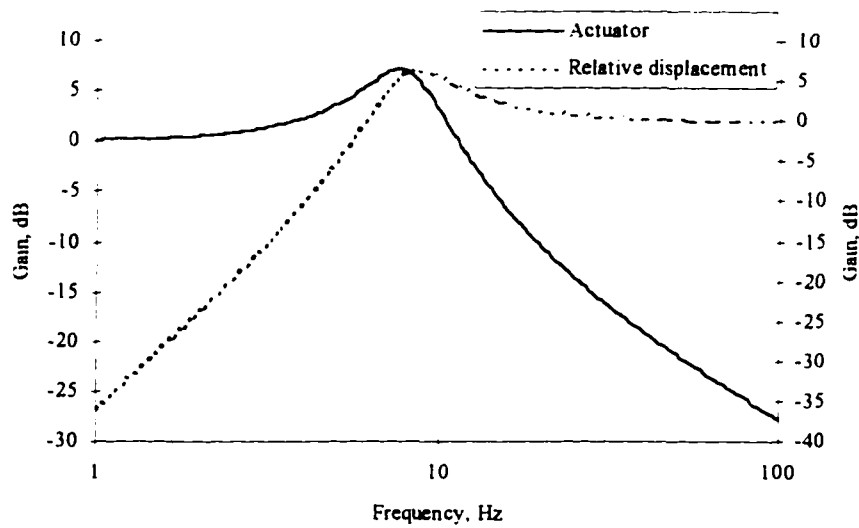


Fig. 2.13 Magnitude Bode plot of the response of the actuator and relative displacement of the lens for the shock and vibration.

The total transfer function of shock and vibration is equal to the cascade combination of the shock mount and the relative lens displacement transfer function. The amplitude Bode plot of the cascade combination of shock mount and actuator model is shown in Fig. 2.14.

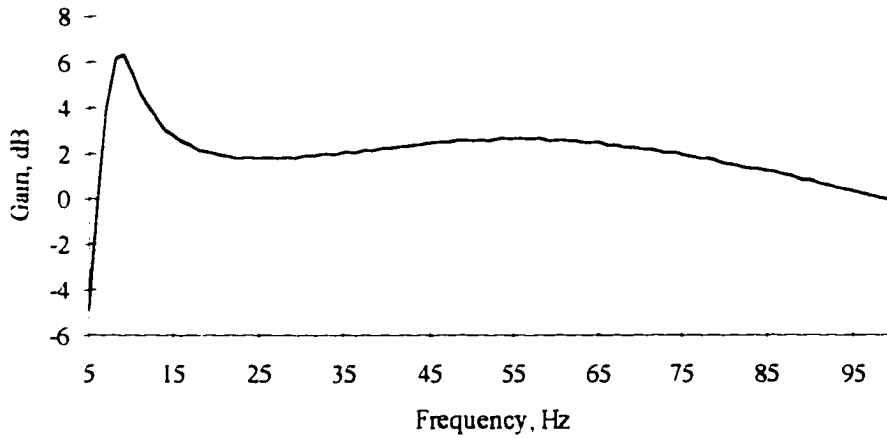


Fig. 2.14 Magnitude Bode plot of actuator and shock mount

We can determine the response of the system (uncorrected acceleration error) without servo control by multiplying the input power density and the total transfer function of shock and vibration. This response is our uncorrected acceleration error, a_i . The uncorrected acceleration error in terms of displacement x_i can be represented as $s^2 \cdot x_i$. The corrected acceleration error, a_o , to shock and vibration using our designed servo system transfer function for error rejection $T_e(s)$ is,

$$a_0(s) = T_e(s)a_i(s) \quad (2.26)$$

Eq. (2.26) in terms of displacement is,

$$x_0(s) = \frac{T_e(s)}{s^2} a_i(s) \quad (2.27)$$

As the above equations show, the corrected displacement error (x_0) is obtained by double integration of the error rejection transfer function with respect to frequency. For an acceleration input, we define the error rejection function, $C(s)$ as,

$$C(s) = \frac{T_e(s)}{s^2} \quad (2.28)$$

The amplitude Bode plot of $C(s)$ is shown in Fig. 2.15.

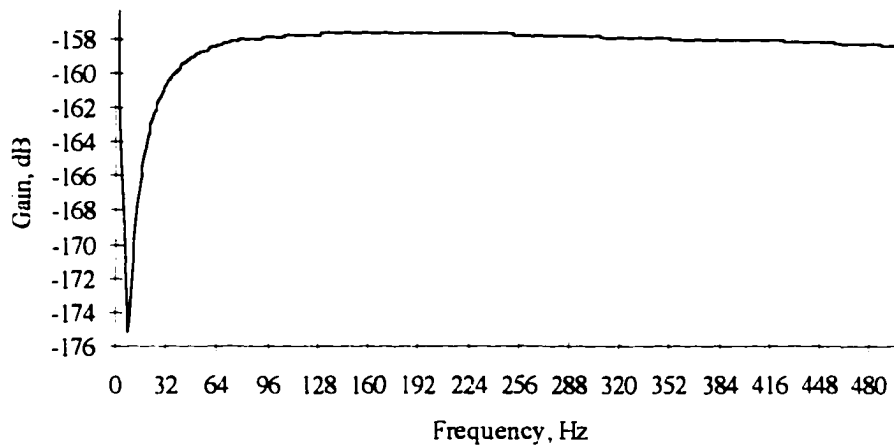


Fig. 2.15 Bode plot of the accelerated error rejection

At low frequencies, the error rejection ability increases as the frequency increases up to the resonant frequency (8 Hz). At frequencies higher than the resonant frequency, the error rejection ability decreases quickly until it reaches an almost constant value of -158 dB.

The power density spectrum of the corrected error rejection is equal to the input power density multiplied by the squared multiplication of the absolute value of the shock, the relative displacement of the lens $G_b(s)$ and the error rejection function $C(s)$,

$$PSD(s) = Vib \cdot (3 \cdot 10^6 \cdot 9.8 \cdot |(Shock(s) \cdot G_b(s) \cdot C(s))|)^2 \quad (2.29)$$

The factor of three is to evaluate 3σ , the factor of 9.8 converts G's of the input power density to meter per second squared and 10^6 converts meters to microns. The total RMS value of the 3σ corrected error for the shock and vibration of the response focus servo is,

$$Error = \sqrt{\int_5^{500} PSD df} \quad (2.30)$$

The corrected error from Eq. (2.30) is 0.217 microns which is less than our specification (0.346 μm). This concludes that our focus servo design is capable of reducing the shock and vibration disturbance to an acceptable amount. The plot of the power density versus frequency is shown in Fig. 2.16. Fig. 2.16 shows that a large part of the error is accumulated in the frequency range of 45 to 65 Hz. The error in the frequency range from 40 to 65 Hz is,

$$Error = \sqrt{\int_{40}^{65} PSDdf} = 0.173 \mu m \quad (2.31)$$

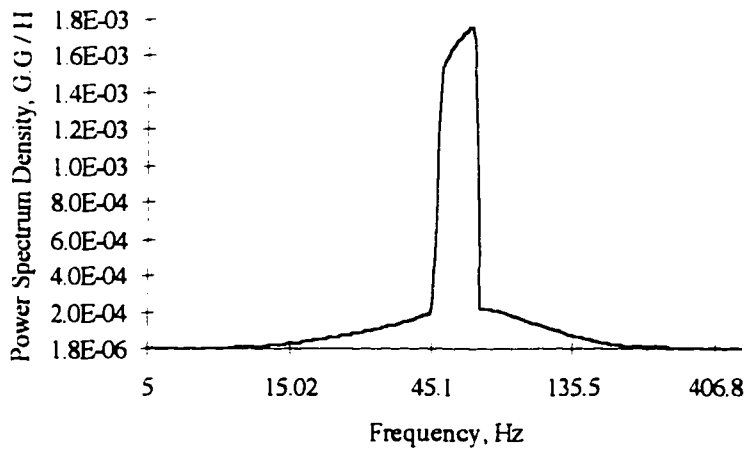


Fig. 2.16 Power density spectrum for closed-loop system

2.6 Summary

In this chapter we provided FMR specifications, disk runout specifications, and design target specifications for our proposed focus servo control system. We established a total FMR budget. We presented models for the focus actuator and the shock mount. The frequency domain analyses of these models were developed to study resonance and their effects on the performance of the control system. The details of the modeling work and the specific parameter values that were used for the controller design were given. We determined the required servo bandwidth by using a compensator and integrator controller to reduce the focus error to our design target in the presence of the disk runout disturbance. We showed that our servo design with the specified bandwidth can also reduce the disturbance due to shock and vibration to an acceptable amount.

CHAPTER 3

3. DIGITAL CONTROLLER DEVELOPMENT

In this chapter, we explore the design compromises imposed by digital controllers. Section 3.1 presents the issues that arise when implementing digital control designs that are of no significance when designing analog controllers. Section 3.2 contains the discrete models of the actuator, compensator, and integrator. Section 3.3 describes the transient response and the steady state error of the focus servo loop. In Section 3.4 we summarize our work.

3.1 Issues of Importance in Digital Controller Implementation

Although many of the design concepts from the analog setting extend into the digital setting, there are additional issues that must be addressed

when designing digital controllers. These additional issues, which are not found in the analog design, serve to make the digital controller design more challenging than the analog controller design. The issues that arise in the digital setting consist of: (i) sample rate selection, (ii) determination of the anti-aliasing filters, (iii) selection of A/D and D/A converters, (iv) addressing computation time delay, and (v) scaling control law variables. The remainder of this section will address each of these issues

3.1.1 Sample Rate Selection

The sampling period was chosen based on the stability and overall performance of the digital control system. The choice of the sampling rate depends on many interrelated factors, such as the closed-loop speed of the process to be controlled, the choice of anti-aliasing filter, the high frequency unmodelled dynamics of the system, and the cost of the digital hardware used to implement the control law such as DSP, A/D, and D/A. The sampling rate has an effect on the phase margin, a faster sampling rate produces a smaller

phase delay which increases the phase margin. Typically, the sampling rate is selected to be 10 to 20 times faster than the closed-loop bandwidth [7]. The sampling period needs to be large enough to encompass the control law computation time and other DSP operations.

The Nyquist theorem requires that at a minimum, the sampling rate must be greater than two times the system bandwidth. If this condition is not met, the result will be an aliased version of the closed-loop roots which may lead to unwanted response characteristics [7].

The controller usually has been designed to increase the damping in high frequency (resonant modes) unmodelled dynamics, then the sampling rate should be selected to be at a rate that is greater than twice the resonant frequency under consideration.

The determination of anti-aliasing filters is closely related to selection of a sampling rate. To select a sampling rate for our servo loop, we designed an anti-aliasing filter that met our design specification for phase margin ($\approx 45^\circ$).

With all of the above considerations, the slowest sampling rate that met all of the performance specifications was determined to be 100 kHz (see Section 3.1.3 and 3.1.4).

3.1.2 Determination of the Anti-Aliasing Filter

The anti-aliasing filter bandwidth is related to the sampling rate and for an ideal low pass filter the cut-off frequency is equal to half of the sampling frequency. The impact of the anti-aliasing filters upon the control design is mainly through the additional phase-lag introduced into the system.

The anti-aliasing bandwidth is selected to be 50 kHz (ω_1) with a damping factor, $\zeta_1=0.5$. This analog filter bandwidth results in approximately 3° of phase delay at 2.7 kHz, which is acceptable for our design. Any bandwidth less than 50kHz results in an unacceptable phase delay. The anti-aliasing filter specifications are shown in Table 3.1. The transfer function for the anti-alias filter is,

$$G_1(s) = \frac{\omega_1^2}{s^2 + 2\zeta_1 s + \omega_1^2} \quad (3.1)$$

The amplitude and phase Bode plots of the anti-aliasing filter are shown in Fig. 3.1. The digital representation of the anti-alias filter is determined from the pole zero mapping technique [8]. To have the true representation of the analog filter during the digital frequency domain modeling, the filter is digitized in the model at a rate that is 100 times faster than the sampling rate. If we were to digitize the filter at 10 MHz, there would not be any difference in the phase response between the analog and digital representations. In Section 3.2.3, we will simulate the digital model of the whole focus servo system with a sampling rate of 10 MHz to find the phase margin of the control system. With such a fast sampling rate, we will represent the true behavior of the two analog components, actuator and low pass filter in the digital frequency domain.

Table 3.1 Anti-aliasing filter

DESCRIPTION	NOTATION	VALUE
Bandwidth	BW_1	50 kHz
Damping factor	ζ_1	0.5
Phase loss	$\theta_1 @ 2.7 \text{ k Hz}$	3°

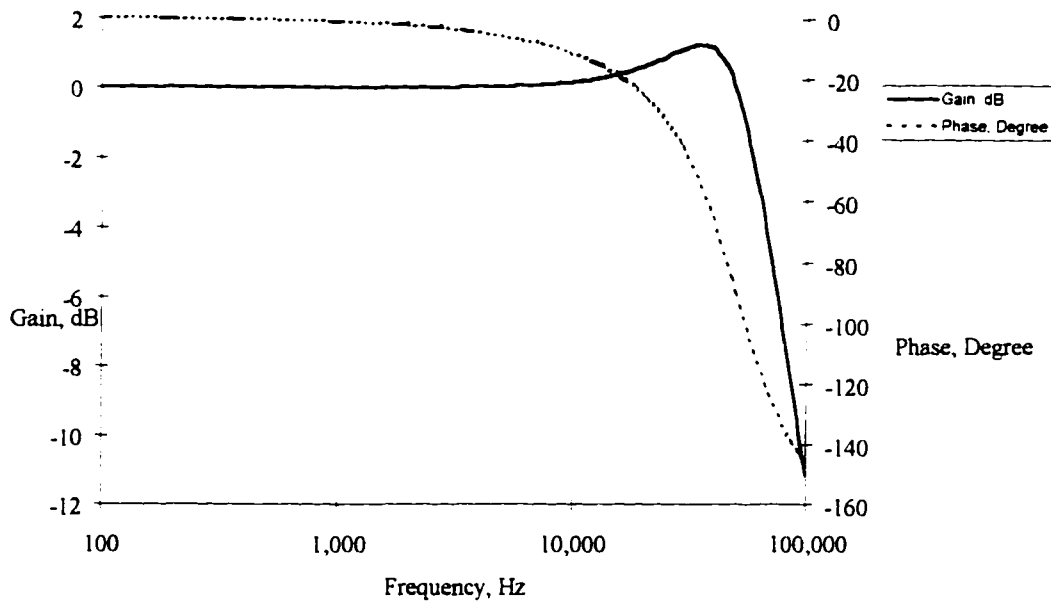


Fig. 3.1 Bode plots of the anti-aliasing filter

3.1.3 A/D and D/A Converters

The selection of the A/D and D/A converters centers around two issues. One is the time required to perform the A/D conversion process and the other is the amount of resolution that is required from the converters. The conversion time for the A/D and the D/A converters is not addressed in this report because it is a cost versus performance issue.

In general, the D/A converter can be modeled as a hold circuit that holds the converted value constant for one sampling period. The D/A converter is commonly modeled as a zero-order hold. It accepts a unit pulse sample at some multiple of the sampling rate, $t = kt_s$, and holds its output constant at this value until the next sample is sent at $t = kt_s + t_s$. The amplitude and phase Bode plots of the zero-order hold in the analog domain are shown in Fig. 3.2. The phase delay produced by the zero-order hold with a 100 kHz sampling rate is 4.8° at a servo bandwidth frequency of 2.7 kHz. A slower sampling rate would result in a larger phase delay for the zero order hold. For example, a 10 kHz sampling rate would result in 48° phase delay at the servo bandwidth frequency. The servo bandwidth requires us to use a sampling rate of 100 kHz or greater, in order to achieve an acceptable phase delay of 4.8° , for the zero-order hold.

The dynamic range of the D/A converter is based on the disk runout, $E_{uc} = \pm 200 \mu\text{m}$, and the system tolerance, $E_s = \pm 200 \mu\text{m}$. Therefore, the total dynamic range is $\pm 400 \mu\text{m}$. The quantization level or resolution of D/A is selected to one tenth of the corrected error for the disk runout, $E_c = 0.346 \mu\text{m}$.

We have the total number of quantization steps to be equal to $400/0.0346=11560$. This number of steps can be represented with 14 bits. From this reasoning the D/A is determined to use 13 bits plus 1 sign bit.

Fig. 1.2 shows that the signal out of the focusing sensor is input to the A/D. The “S”-curve for the focusing sensor is defined as a change in the focus error signal as the objective lens is moved through focus [3]. The “S”-curve for the focusing sensor converts the actuator displacement (x_0) into a voltage signal which is sampled by the A/D. The total dynamic range of the focusing sensor is $\pm 20 \mu\text{m}$ with a 20% tolerance yielding a total of $\pm 24 \mu\text{m}$. The quantization level (resolution) of the A/D is selected to be $0.01 \mu\text{m}$ which results in $24/0.01=2400$ quantization steps. A 12 bit A/D converter can represent the total dynamic range of the focusing sensor. We determined to utilize a 12 bit A/D converter with sampling capability of 100 kHz.

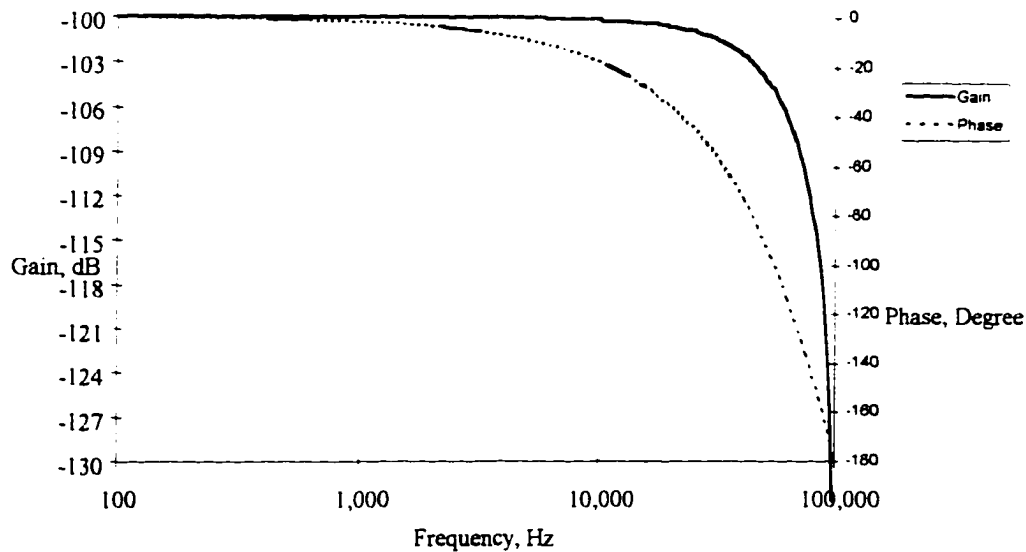


Fig. 3.2 Bode plots of the zero-order hold

3.1.4 Addressing Computation Time Delay

We selected the computation delay for the DSP and A/D converter to be equal to 80% of the sampling period ($T_{\text{compute}} = 8 \mu\text{s}$). This leaves 20% of the DSP's operation time to perform communication and other overhead operations. The loss in phase margin due to finite computation time of the DSP is,

$$\theta_{loss}(s) = \frac{T_{compute}}{T(s)} \cdot 360 \quad (3.2)$$

The above equation is derived from setting the ratio of the phase loss at the frequency of interest, s , to the phase of one period (360°) equal to the ratio of the computation time to the period of the frequency of interest, $T(s)$. A plot of the phase delay due to computation as a function of frequency is shown in Fig. 3.3. With a sampling rate of 100 kHz, Fig. 3.3 shows a phase delay of 7.8° at the servo bandwidth frequency. A slower sampling rate will produce a larger phase delay because $T_{compute}$ is assumed to be a fixed percentage of the sampling period.

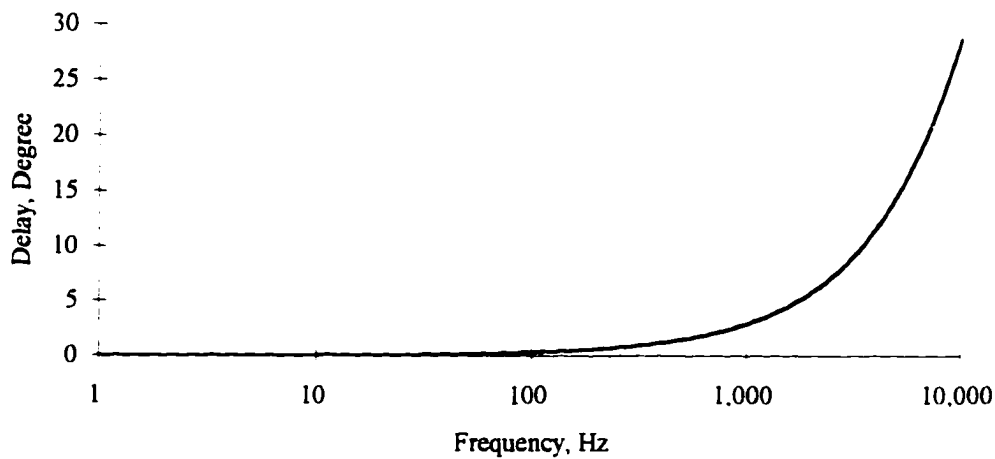


Fig. 3.3 Computation delay phase for a sampling rate of 100 kHz

3.1.5 Scaling the Control Law Variables

The scaling of signals into and out of the DSP may not be as important to the designer if the DSP has floating point arithmetic. However, most control applications can be realized with a fixed point DSP if the signal scaling is adequately addressed. A fixed point DSP will be less expensive and typically allows for faster processing speed, which are two significant features that favor its use.

The overall goal of the scaling operation is to have all of the signals inside the control law bounded between ± 1 (where the value of 1 is represented by the maximum word length plus a sign bit in the DSP) to minimize the occurrence of an overflow condition. In Section 3.2.1, we will describe the discrete models of the compensator and integrator with coefficients less than 1 for scaling purposes.

3.2 Discrete Models of the Controller and the Actuator

In this chapter, we will present the discrete models of the compensator, the integrator, and the actuator in the frequency domain. We will also look at the digital modeling of the whole system. In Sections 3.1.2 and 3.1.3, the design of the anti-aliasing filter and zero order hold system provided insight into how the digital implementation issues such as sampling rate and phase delay influence the closed-loop system performance.

A block diagram of the digital focus servo for the actuator motion is shown in Fig. 1.2. The analog components, actuator and anti-aliasing filter,

and the digital component, DSP, are interfaced through the A/D and D/A converters. The DSP controller implements the lead compensator and the integrator.

3.2.1 Discrete Models of the Compensator and Integrator

The digital transformation of the compensator Eq. (2.13)without the constant gain K_c is

$$G_c(z) = \frac{y_c}{x_c} = \frac{b_0(z - \frac{b_2}{b_0})}{(z - a_1)} \quad (3.3)$$

where a_1 and b_2 are calculated using pole zero mapping techniques and b_0 for scaling purposes is set to 0.5. b_2 is given by,

$$b_2 = e^{-2\pi f_{zw} t_s} \cdot b_0 \quad (3.4)$$

and a_1 is given by,

$$a_1 = e^{-2 \cdot \pi \cdot f_{pw} \cdot t_s} \quad (3.5)$$

f_{pw} and f_{zw} are the prewarped critical s-domain frequencies [8]. The defined prewarped pole and zero frequencies are,

$$f_{pw} = \frac{2}{t_s} \tan\left(\frac{f_p t_s}{2}\right), \quad (3.6)$$

and

$$f_{zw} = \frac{2}{t_s} \tan\left(\frac{f_z t_s}{2}\right), \quad (3.7)$$

where f_p is 10.5 kHz , and f_z is 700 Hz for the analog lead compensator.

The sampling period, t_s is 10 μ s. The block diagram of the digital implementation of the compensator is shown in Fig. 3.4. For the software implementation of the digital compensator, its z-transform needs to be converted to a difference equation [8]. The difference equation for the compensator is,

$$y_c(k) = -b_2 \cdot x_c(k-1) + b_0 \cdot x_c(k) + a_1 \cdot y_c(k-1), \quad (3.8)$$

where $x_c(k)$ is the difference between the FES reference input and the discrete output of the A/D. $y(k)$ is the discrete output of the DSP that is sent to the actuator according to the block diagram shown in Fig. 1.2. For this design, the coefficients are given in Table 3.2.

Table 3.2 Compensator parameters

COMPENSATOR PARAMETERS	
PARAMETER	VALUE
b_2	0.945
a_1	0.319
b_0	0.5

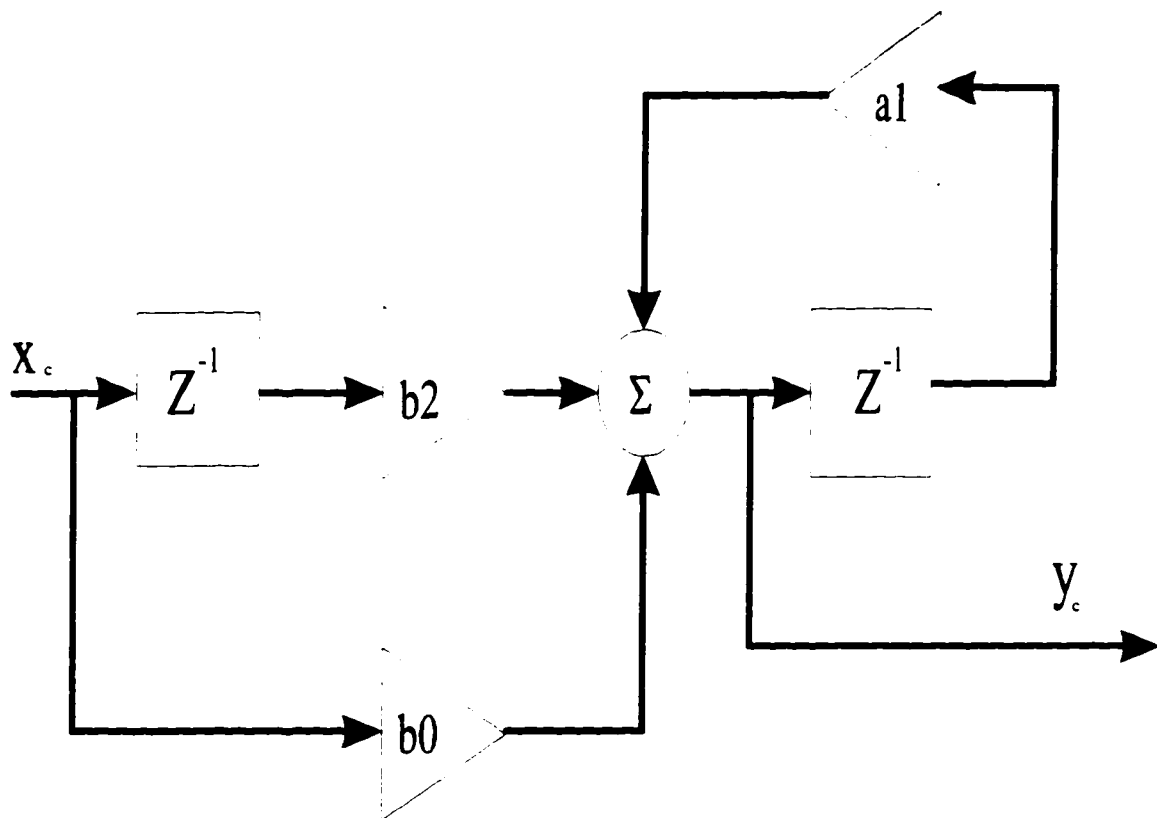


Fig. 3.4 Block diagram of the lead compensator

The Bode plots of gain and phase of the compensator for the analog and digital implementations are shown in Fig. 3.5 and Fig. 3.6, respectively. Similar performance between the analog and digital implementation is observed up to the sampling rate, t_s .

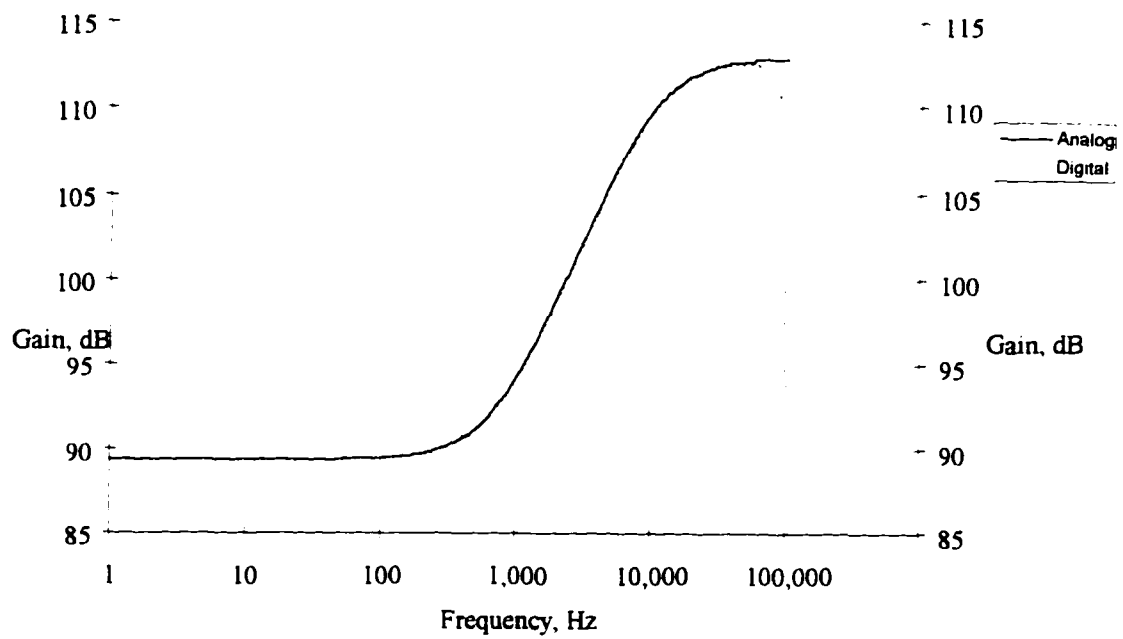


Fig. 3.5 Magnitude Bode plot of the compensator

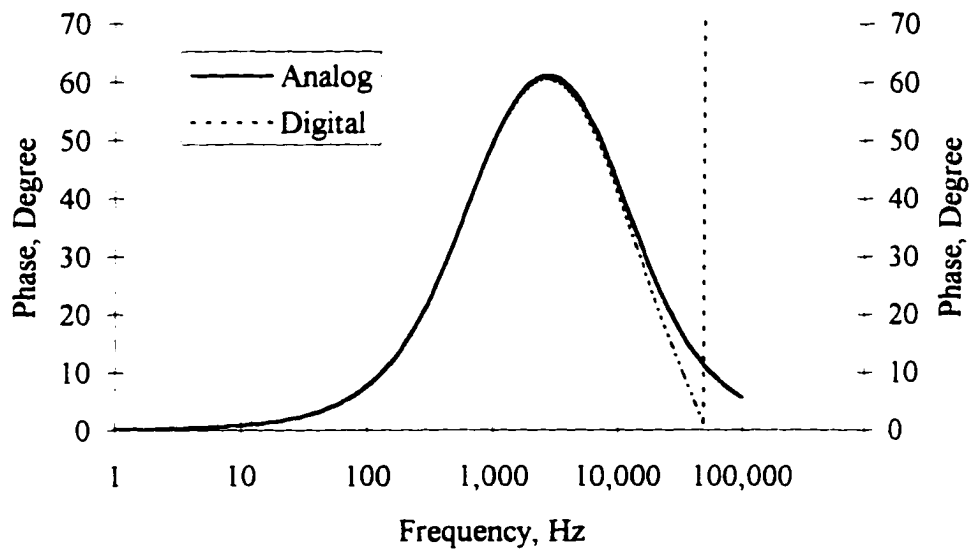


Fig. 3.6 Phase Bode plot of the compensator

The block diagram of digital design of the integrator is shown in Fig. 3.7. Half of the output of the compensator goes into the integrator and the other half sums up with the output of the integrator. The integrator is designed to allow the DSP to bypass the output of the integrator every other sample for computation efficiency. The z-transform of the integrator shown in Fig. 3.7 is,

$$y_i = \left(b_i - \frac{a_i}{2}\right) \frac{x_i}{2} z^{-1} + \frac{x_i}{2} + \frac{a_i}{2} z^{-1} y_i \quad (3.9)$$

where x_i is the output of the compensator (input to the integrator) and y_i is the output of the integrator. The coefficients of the integrator in Eq. (3.9) are given in Table 3.3.

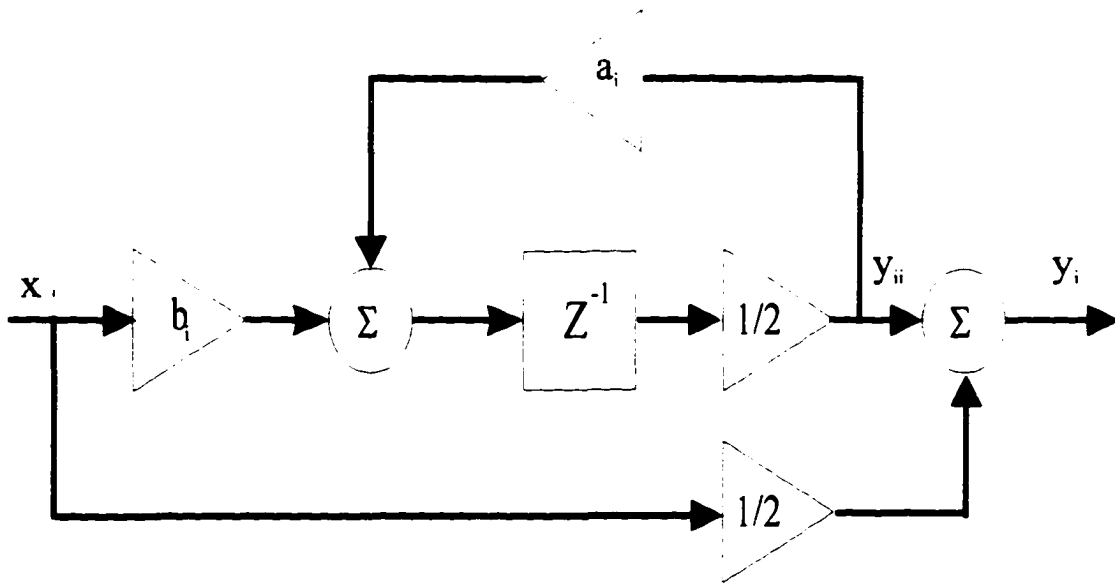


Fig. 3.7 Block diagram of the integrator

The digital transfer function of the integrator derived from Eq. (3.9) is,

$$G_i(z) = \frac{y_i}{x_i} = \frac{1}{2} \left[\frac{z - \left(\frac{a_i}{2} - b_i \right)}{z - \frac{a_i}{2}} \right] \quad (3.10)$$

The pole, $a_i/2$ of the z transfer function of the integrator using the pole/zero transformation technique from the analog to the digital domain is,

$$\frac{a_i}{2} = e^{-2 \cdot \pi \cdot f_{pi} \cdot t_s} \quad (3.11)$$

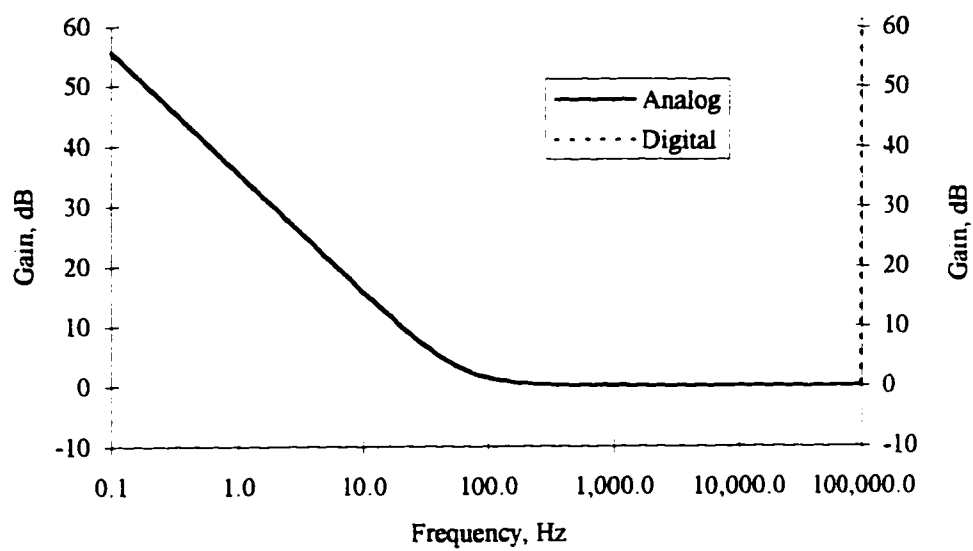
where f_{pi} is the corresponding analog domain pole (0.1 Hz). For low frequencies, the prewarped frequency correction is not necessary. With a_i calculated, the zero, $(\frac{a_i}{2} - b_i)$, is used to determine b_i , thus

$$b_i = \frac{a_i}{2} - e^{-2 \cdot \pi \cdot f_{zi} \cdot t_s}, \quad (3.12)$$

where f_{zi} is the corresponding analog domain zero (30 Hz). The Bode plots of the gain and the phase of the integrator for the analog and digital implementations are shown in Fig. 3.8 and Fig. 3.9, respectively. Similar performance between the analog and digital implementation is observed up to the sampling rate.

Table 3.3 Integrator parameters

INTEGRATOR PARAMETERS	
PARAMETER	VALUE
a_i	2.0
b_i	0.002

**Fig. 3.8** Magnitude Bode plot of the integrator

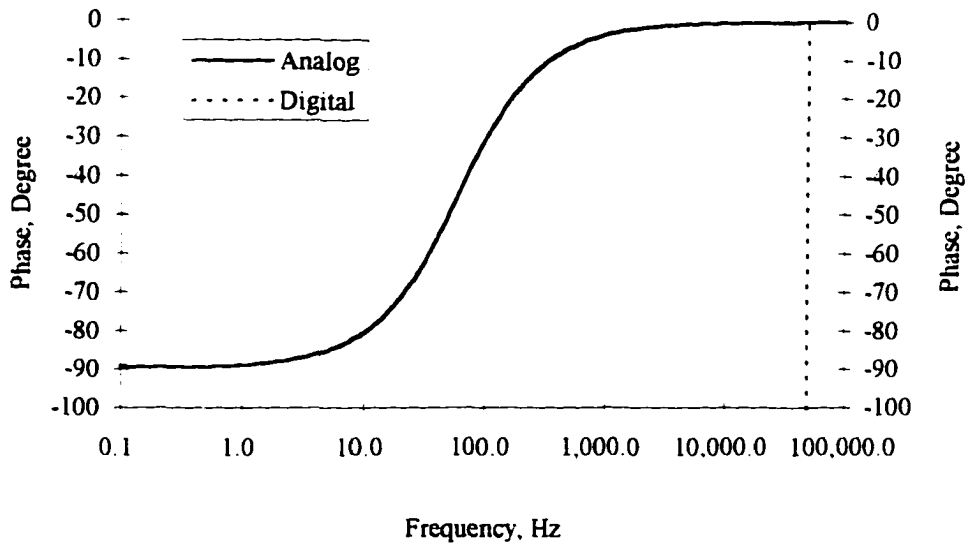


Fig. 3.9 Phase Bode plot of the integrator

The cascade combination of the compensator and the integrator is

$$G_t(z) = G_c(z) \cdot 2 \cdot G_i(z), \quad (3.13)$$

where the multiplication by the factor of two is necessary because only half of the output of the compensator is utilized by the integrator. The inputs to the last summing junction shown in Fig. 3.7 are each scaled by a factor of $\frac{1}{2}$ to

prevent an overflow condition ($|y_i| > 1$) from occurring. From the block diagram shown in Fig. 3.7 we can see that y_i is equal to only one half of the output of the compensator when y_{ii} is equal to zero. y_{ii} is equal to zero if the steady state error is zero or if the integrator is disabled by the DSP. From this reasoning the factor of two shown in Eq. 3.13 is justified. The magnitude and phase Bode plots for both the analog and digital implementations are shown in Fig. 3.10 and Fig. 3.11, respectively.

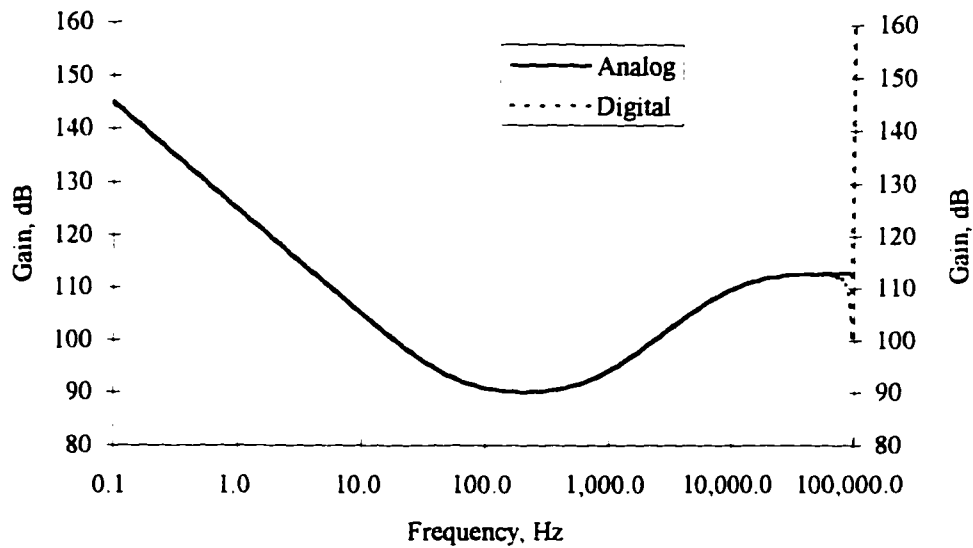


Fig. 3.10 Magnitude Bode plot of the compensator and integrator

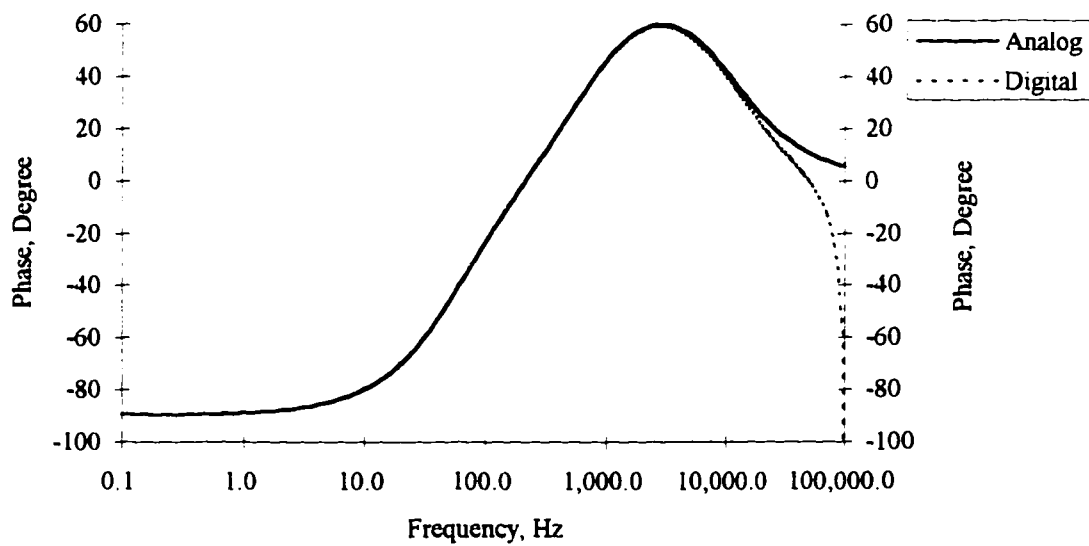


Fig. 3.11 Phase Bode plot of the compensator and integrator

3.2.2 Discrete Model of the Actuator

The actuator is an analog component of the digital focus servo control system. Fig. 1.2 shows that the actuator is placed between the DAC and the ADC. We wish to find the discrete transfer function $G_a(z)$ of the actuator, when the continuous transfer function is $G_a(s)$. For the digital frequency domain modeling of the whole system, which consists of analog and digital components, we need a simulated sampling rate, T , that is 100 times faster than our real sampling rate, t_s , in order to achieve an accurate representation of the actuator as we did for the anti-aliasing filter.

One issue that we need to be concerned with is that a faster sampling rate will result in a smaller phase delay for our digital components such as the zero-order hold. This will not represent the real behavior of our system during digital modeling. For digital modeling with a faster sampling rate, T , we need to delay the zero-order hold by the same integer factor (100 times) to compensate for the increased sampling rate. This allows us to achieve the same phase delay for the digital components that the real operating system has.

The D/A converter accepts a sample pulse $u(kT)$ at $t = kT$. To delay its output, we need to hold it constant at this value until the next sample is sent at $t = 100 \cdot kT + T$. Therefore the output of the D/A converter is a pulse of width $100 \cdot T$ seconds and a height of $u(kT)$. Mathematically, this pulse is given by, $u(t) - u(t - 100 \cdot T)$. The response is the difference between the step response (to $u(t)$) and the delayed step response (to $u(t - 100 \cdot T)$). The Laplace transform of the step response is $G_a(s)/s$. Thus in the frequency domain, the transfer function between the actuator and the zero-order hold is,

$$\frac{x_o(s)}{e(s)} = (1 - e^{-100 \cdot T \cdot s}) \cdot \frac{G_a(s)}{100 \cdot s}, \quad (3.14)$$

and the discrete transfer function of the actuator and zero-order hold is,

$$G_a(z) = (1 - z^{-100})Z\left\{\frac{G_a(s)}{100 \cdot s}\right\}. \quad (3.15)$$

We now consider computing the discrete transfer function of the computation delay. T_{compute} is 80% of the sampling interval. The computation transfer function in the s-domain is,

$$G_{\text{compute}}(s) = e^{-T_{\text{compute}} \cdot s} \quad (3.16)$$

T_{compute} is defined as,

$$T_{\text{compute}} = l \cdot t_s - m \cdot t_s, \quad (3.17)$$

where l is an integer ($l=1$) and m is a positive number less than 1.0 (0.2).

With these definitions we can write,

$$G_{\text{compute}}(s) = e^{-l \cdot t_s \cdot s} \cdot e^{m \cdot t_s \cdot s} \quad (3.18)$$

Substituting for t_s in Eq. (3.18) we obtain,

$$G_{compute}(s) = e^{-100l \cdot T \cdot s} \cdot e^{100m \cdot T \cdot s} \quad (3.19)$$

Taking the z transform of Eq. (3.19),

$$G_{compute}(z) = z^{-100l} \mathbf{Z} \left\{ e^{100m \cdot T \cdot s} \right\} \quad (3.20)$$

Because l is an integer, the term e^{-lTs} reduces to z^{-l} when we take the z -transform. Because $m < 1$, the transform of the other term is quite direct.

The discrete transfer function of the actuator, zero-order hold, and computation delay, $G_{ad}(z)$, is,

$$G_{ad}(z) = (z^{-100l}) \cdot (1 - z^{-100}) \mathbf{Z} \left\{ \frac{e^{100mT \cdot s} \cdot G_a(s)}{100s} \right\}. \quad (3.21)$$

We know the actuator transfer function $G_a(s)$ Eq. (2.2) and, after the partial fraction expansion of $G_a(s)/s$, we have,

(3.22)

$$G_{ad}(z) = \frac{z^{100} - 1}{100 \cdot z^{100 \cdot l + 100}} Z \left\{ \frac{M_0 \cdot e^{100 \cdot m \cdot T \cdot s}}{s} + \frac{M_1 \cdot e^{100 \cdot m \cdot T \cdot s}}{s + \omega_{a1}} - \frac{M_2 \cdot e^{100 \cdot m \cdot T \cdot s}}{s + \omega_{a2}} \right\},$$

where ω_{a1} and ω_{a2} are the complex poles of the actuator. The coefficient M_0 , M_1 , and M_2 are,

$$M_0 = \frac{K_a}{(\omega_{a1} \cdot \omega_{a2})}, \quad (3.23)$$

$$M_1 = \frac{K_a}{\omega_{a1}^2 - \omega_{a1} \cdot \omega_{a2}}, \quad (3.24)$$

$$M_2 = \frac{K_a}{-\omega_{a2}^2 + \omega_1 \cdot \omega_{a2}}, \quad (3.25)$$

where K_a is the normalized gain of the actuator. K_a is $2527/\text{sec}^2$,

To complete the transfer function, we need the z -transforms of the inverses of the terms in the braces. The first term is a unit step shifted left by $100mT$ seconds ($2 \mu\text{s}$), and the last two terms are exponential functions shifted left by the same amount. Because $100mT$ is $2 \mu\text{s}$, these shifts are less than one full period of the real sampling period ($10 \mu\text{s}$), and no samples are picked up in negative time.

The final z -transform of the actuator including the zero-order hold and computation delay is,

(3.26)

$$G_{ad}(z) = \frac{z^{100} - 1}{100 \cdot z^{100/l + 100}} \left\{ \frac{z}{z-1} + \frac{M_1 \cdot z \cdot e^{100 \cdot m \cdot T \cdot s}}{z - e^{-\omega_{a1} \cdot T}} - \frac{M_2 \cdot z \cdot e^{100 \cdot m \cdot T \cdot s}}{z - e^{-\omega_{a2} \cdot T}} \right\}$$

The magnitude and phase Bode plots of the actuator transfer function including the zero-order hold and the computation delay in analog and digital domain are compared in Fig. 3.12 and Fig. 3.13, respectively. The magnitudes of the analog and digital domain of the actuator transfer function are the same up to the sampling rate. As we expected, the digital representation of the actuator has a phase delay of 12.6° at the crossover frequency which is the same as the analog representation. 12.6° is the summation of the zero-order hold delay (4.8°) and the computation delay (7.8°) at the crossover frequency.

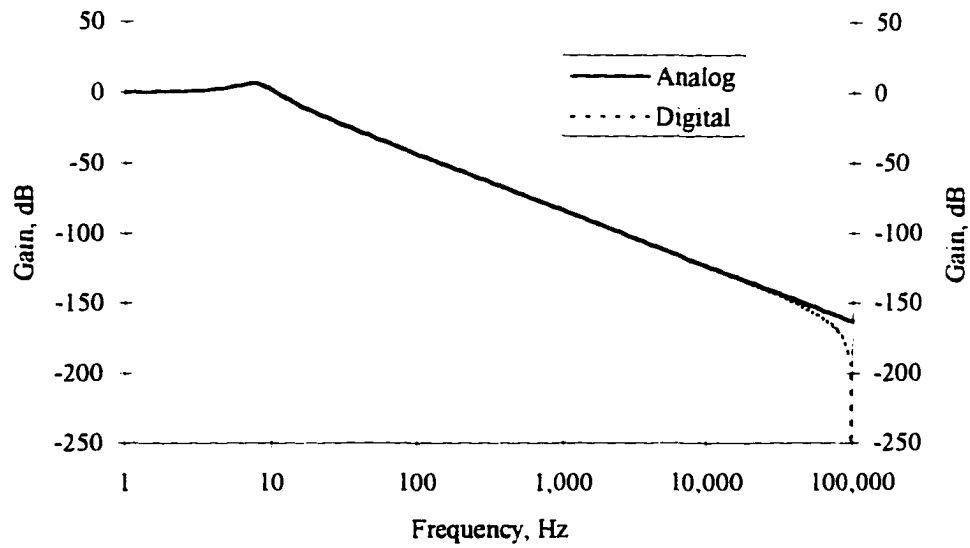


Fig. 3.12 Magnitude Bode plot of the actuator including the zero-order hold and the computation delay

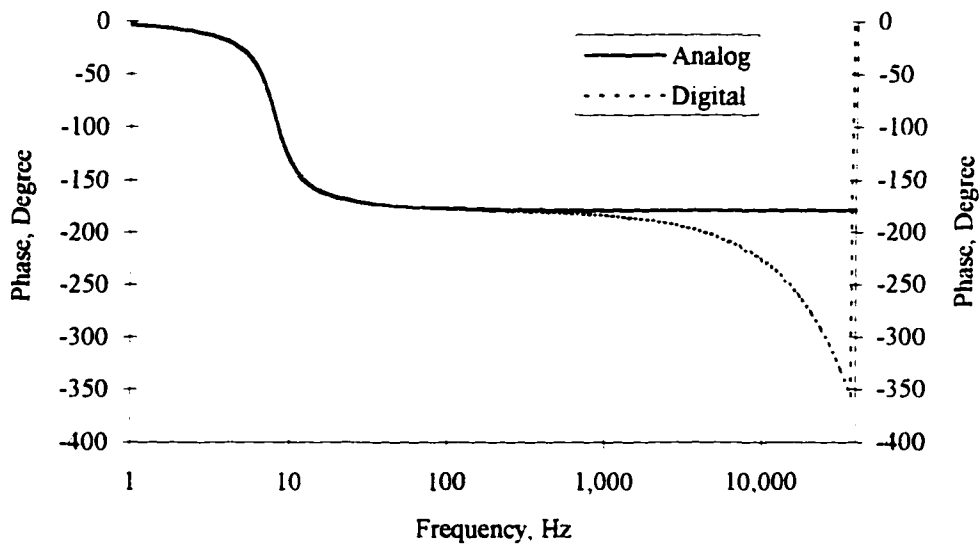


Fig. 3.13 Phase Bode plot of the actuator including the zero-order hold and the computation delay

3.2.3 Digital Modeling of the Whole Focus Servo System

In Section 3.2.3, we derived the discrete transfer function of the actuator at the faster simulation sampling period T , of $0.1 \mu\text{s}$. The discrete transfer function of the actuator and the anti-aliasing filter at this faster simulation sampling rate will represent the true behavior of these analog

components. The appropriate phase delay for the zero-order hold with the sampling rate, t_s is also accurately modeled.

The purpose of the digital frequency domain modeling of the focus servo system at the faster simulation sampling rate is to represent the real focus servo system and to determine its phase margin. To evaluate the phase margin, we need to calculate the open loop discrete transfer function. The open loop discrete transfer function of the focusing servo loop is,

$$G_T(z) = G_c(z) \cdot 2 \cdot G_i(z) \cdot G_{ad}(z) \cdot G_l(z) \quad (3.27)$$

The magnitude and phase Bode plots of the open loop discrete and analog transfer functions (Eq. (2.19)) are compared in Fig. 3.14 and Fig. 3.15, respectively. Fig. 3.15 indicates a phase margin of about 60° for the analog and 45° for the digital modeling representation. The loss of phase margin in the digital representation is due to the zero-order hold and the computation delay.

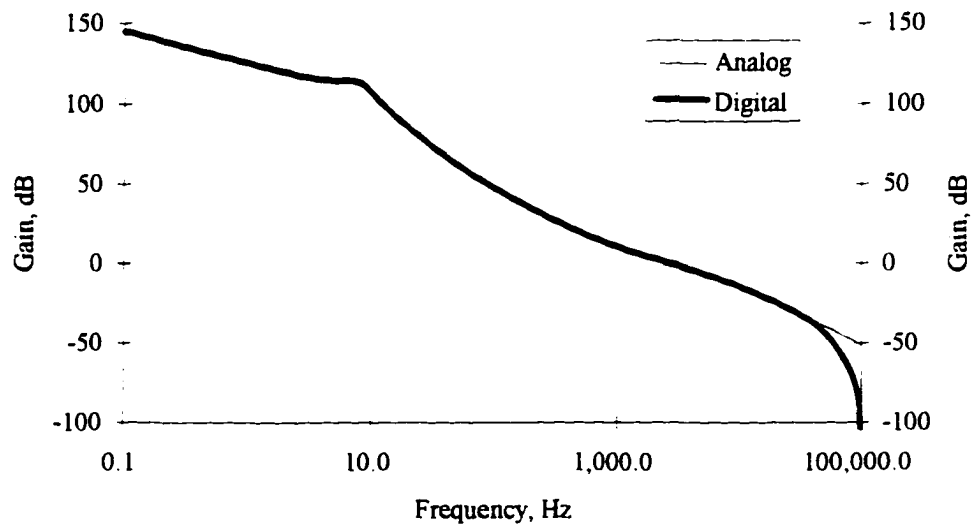


Fig. 3.14 Magnitude Bode plot of the complete open loop transfer function

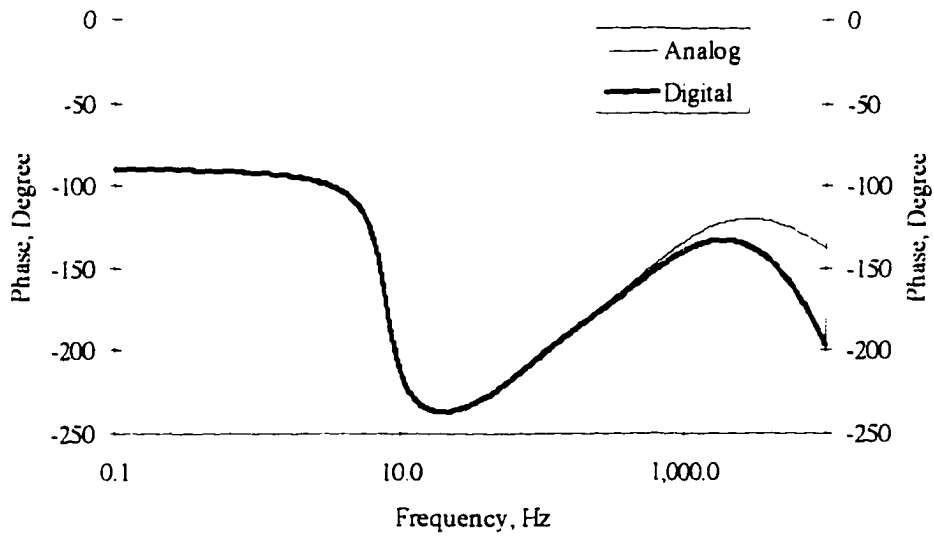


Fig. 3.15 Phase Bode plot of the complete open loop transfer function

The magnitude and phase Bode plots for the closed loop discrete and analog transfer function are shown in Fig. 3.16 and Fig. 3.17, respectively.

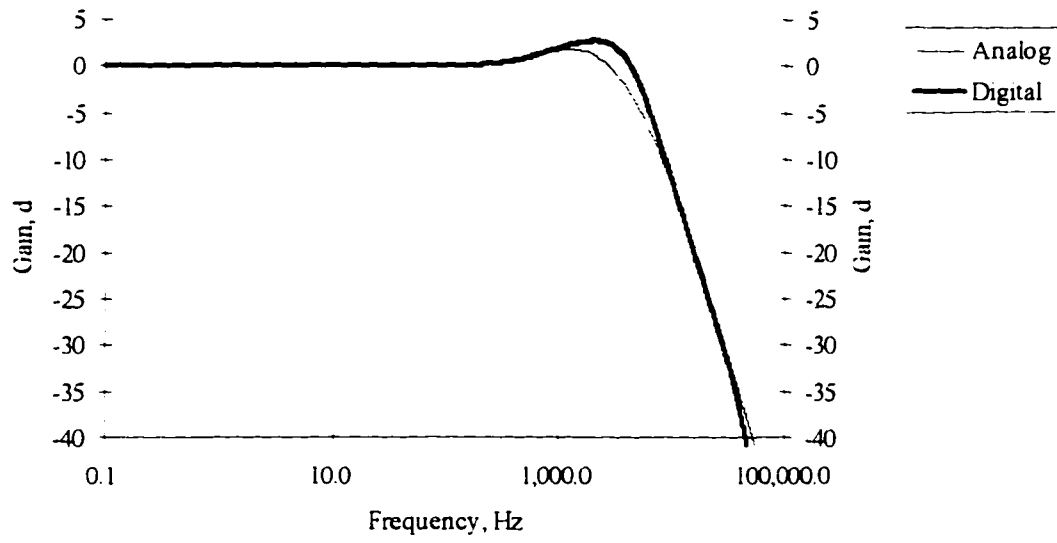


Fig. 3.16 Magnitude Bode plot of the closed loop transfer function

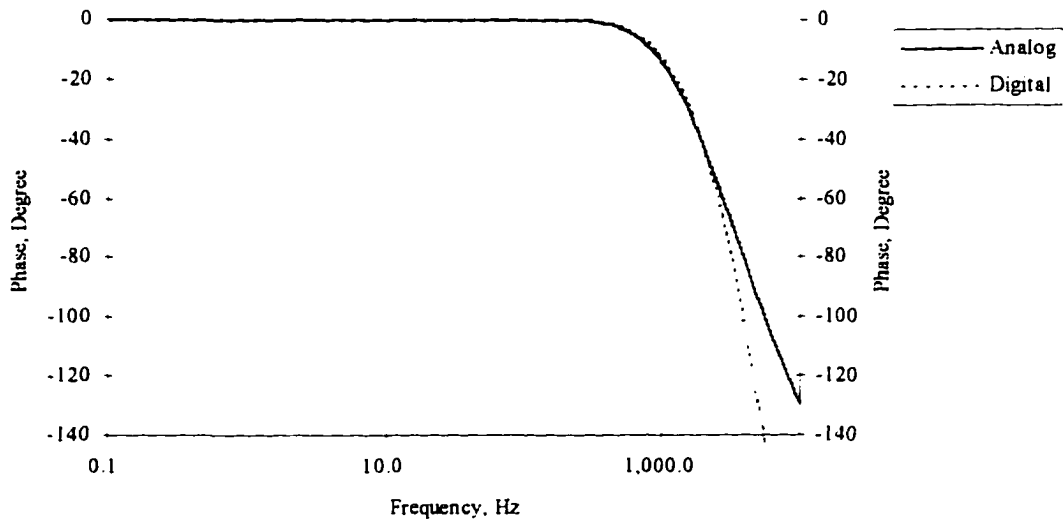


Fig. 3.17 Phase Bode plot of the complete closed-loop transfer function

The peaking between 1 kHz and 2.7 kHz in Fig. 3.16 is inversely proportional to phase margin for the digital and analog representation [9]. Fig. 3.16 has smaller peaking for the analog domain than the digital domain as we expected. The digital representation has a 45° phase margin and 2.6 dB peaking at 2 kHz (see Table 3.5).

3.3 Transient and Steady State Response Analysis

In this section, we will discuss the transient and steady state error response of the closed-loop focus servo control. The transient response refers to the portion of the response due to the closed-loop poles of the system, and the steady state FES response refers to the portion of the response due to the poles of the input or forcing function. It is important to study the time response of the digital control system, which consists of two parts: the transient and the steady state response. To predict the dynamic behavior of our digital closed loop system, we will subject the system to an input in the time domain. The output of the focus servo system cannot follow the input immediately, but exhibits an oscillatory transient response before a steady state can be reached. If a transient response stays oscillatory, the control system is unstable.

We will consider the response of the discrete-time system to time-domain inputs such as a unit step and a sinusoidal with sweeping frequency inputs.

3.3.1 Transient Response and Steady State Error

The discrete closed-loop transfer function of the servo system is now reevaluated at the real system sampling rate of 100 kHz. The transient response of this closed-loop system to a unit step input applied at the FES set point input is shown in Fig. 3.18. The initial condition assumption is that the system is at rest initially and that the output and all its time derivatives are zero.

The difference equation that is developed from the discrete closed loop control is,

(3.28)

$$y(k) = -\frac{1}{A_7} \{ A_6 y(k-1) + A_5 y(k-2) + (B_4 - A_4) y(k-3) + (A_3 + B_3) y(k-4) + \dots \\ (A_4 + B_4) y(k-3) + (A_3 + B_3) y(k-4) + (A_2 + B_2) y(k-5) + (A_1 + B_1) y(k-6) + \dots \\ B_0 y(k-7) - B_4 x(k-3) - B_3 x(k-4) - B_2 x(k-5) - B_1 x(k-6) - B_0 x(k-7) \}$$

where $y(k)$ is the discrete output of the A/D in Fig. 1.2 and $x(k)$ is the input, FES. The difference equation shows that the closed loop system is a seventh order system. The coefficients of Eq. (3.28) are given in Table 3.4,

Table 3.4 Difference equation coefficients

A_1	0.684
A_2	-4.32
A_3	11.45
A_4	16.25
A_5	13.02
A_6	5.58
A_7	1.0
B_0	2.89E-5
B_1	1.67E-6
B_2	-8.85E-5
B_3	5.63E-5

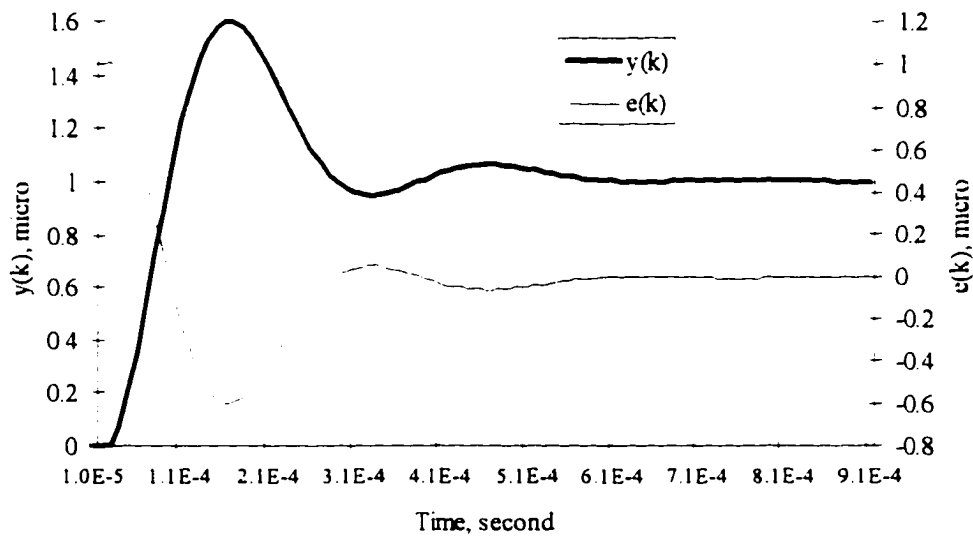


Fig. 3.18 Unit step, transient response and steady state error

The error signal is also shown in Fig. 3.18. The error is defined as,

$$e(k) = FES - y(k). \quad (3.29)$$

FES is equal to one at all times (unit step). The steady state error signal is very close to zero. The transient response has a delay time of $65 \mu\text{s}$, a rise time of $36 \mu\text{s}$, a peak time of $160 \mu\text{s}$, a maximum overshoot of 59%, and a

settling time of 280 μ s. The above transient response can be roughly approximated by a second order model. The phase margin of our digital servo system is 45° which corresponds to approximately a damping factor of 0.45 for the second order system. A second order system damping factor of 0.45 corresponds to a 20% overshoot [9]. The step response in Fig. 3.18 has an overshoot of 59% which corresponds to damping factor of 0.17 or a phase margin of 17° . This overshoot is not what we would expect from our design specifications. This shows that a second order model does not adequately describe the resulting transient performance of our system. This is because of the large amount of phase delay produced in the digital system that reduces our gain margin drastically compared to the analog case.

The transient response and error signal of the digital servo system to a sinusoidal input with a sweeping frequency range of 0 to 10 kHz is shown Fig. 3.19. Fig. 3.19 illustrates what the output and error signal might look like with a varying input frequency. At frequencies higher than our servo bandwidth, the response to sinusoidal input is reduced to zero. It shows that the servo system does not respond to any high frequency disturbances. The

error signal is very small at low frequencies. At frequencies higher than the cutoff frequency, there is no error rejection as expected.

We have summarized the design target and achieved specifications for the digital servo control system in Table 3.5.

Table 3.5 Design target specifications for the digital servo control system

Description	Target	Achieved
Phase margin	45°	45°
Peaking	2.6 dB	2.6 dB
Overshoot	20%	59%

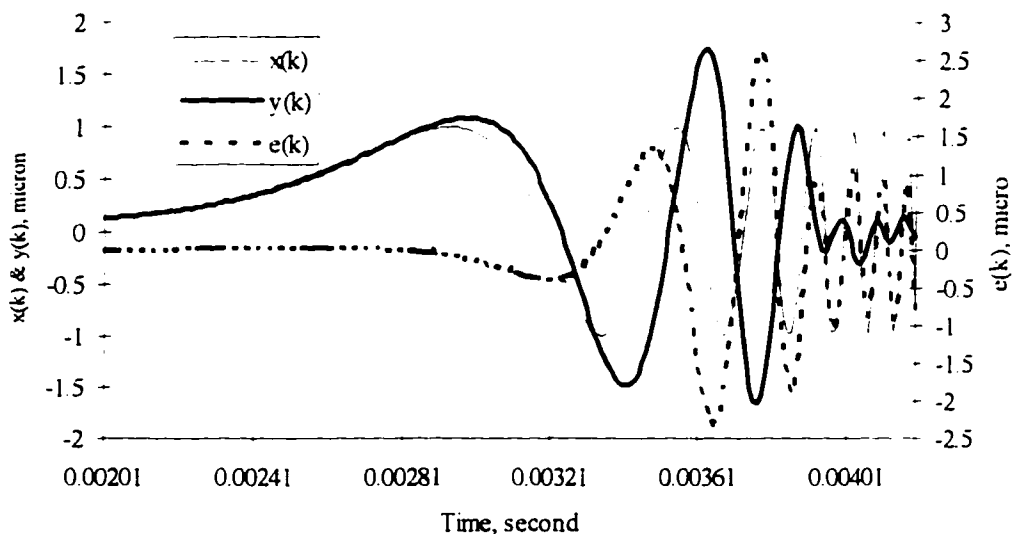


Fig. 3.19 Transient response and error to the sweeping sine wave

3.4 Summary

In this chapter we have shown how the transfer function of analog models represented using the Laplace transform can be described by the z-transform discrete models. The Laplace transfer function of the actuator and the compensator and the integrator are converted to z transforms by using pole zero mapping techniques. The compensator and the integrator transfer functions are normalized for scaling purposes.

A minimum sampling rate was chosen to produce a minimum amount of computation delay and zero order hold phase delay. To have a real representation of the analog components such as the actuator and the anti-aliasing filter, we simulated the whole servo loop at a 100 times faster sampling rate. To achieve the correct zero-order hold phase delay and computation delay during simulation, we delayed the zero-order hold and the computation time by the same integer factor that we used to speed up the sampling rate. We determined the phase margin of the digital system by simulating the whole servo loop at the faster sampling rate. We compared the peaking that we achieved from the simulation in the frequency domain with the overshoot of the transient response in the time domain simulation. The overshoot of the transient response was larger than expected based on a second order model. Therefore we can conclude that the second order model does not adequately describe the resulting transient performance of our system.

CHAPTER 4

4. Summary

In this report, we first analyzed the requirements for a focus servo control system for use in an optical disk tester. We determined a FMR budget that was composed of three dominant components, disk runout, shock and vibration, and system noise. We established a design point for the dynamic performance of the servo system that determined the required phase margin, overshoot, and peaking.

To facilitate our design approach, the specifications of a commercially available focus actuator and a shock mount were used. The frequency domain models of these components were developed from frequency response measurements and parameter estimation to understand their effects on the performance of the control system. A complete analog model of the servo

system in the frequency domain was established to determine an operating design point. The optical disk displacement dynamics information was obtained from ECMA standards associated with the commercial production of magnetic optical disks. Chapter 2 gives the details of the modeling work as well as the specific parameter values that were used for the controller design. We analyzed our analog focus servo control system's ability to operate properly in the presence of expected shock and vibration disturbances.

Since a primary objective of this report is to demonstrate the feasibility of a digital focusing controller for an optical disk tester, some basics on digital controller development and performance details using a frequency-domain approach were given in chapter 3. In particular, certain issues of importance that need to be addressed in the digital control implementation, such as sampling rate, time delay from the zero-order hold model of the D/A converter, and computation delay effects, were discussed. A digital focus control system for use on an optical disk tester was designed based on performance specifications. A digital controller design that met all of the performance requirements was discussed in detail. Modeling and simulation results showed that all of the important performance requirements were

achieved (see Table 3.5) except that the step response overshoot was larger than our design target. The overshoot response possibly could be reduced by increasing the pole/zero separation of the lead compensator. Increasing the pole/zero separation may cause an associated increase in high frequency noise attendant to the increased gain at higher frequencies.

4.1 Future Work

We successfully demonstrated the design procedures for a digital controller implementation for the focusing motion. Specific tasks that need to be investigated in the future are more dependent upon the actual implementation chosen for the servo control system. For example, in the future the availability of less expensive, faster DSPs with less computation time requirements will allow us to operate our focus servo control system with a faster sampling rate. This is only possible if faster ADCs and DACs also become available at lower costs.

Alternative approaches for realizing digital controllers such as hard wired logic (Programmable Gate Arrays) are also possible. The disadvantage

of hard wired logic is that changes or calibration procedures cannot be modified easily. The implementation chosen is dependent upon the schedule and budget requirements. If a DSP approach is chosen, then issues regarding processor selection based on performance, cost, coding efficiency and availability must be considered. In addition, the selection of the ADC and DAC in conjunction with the level of electronic component integration in a single package should be considered. We expect that, in the future, as electronic parts become smaller that the level of integration will increase, thus providing more components located on a single package. This will reduce costs and allow the use of higher performance components.

REFERENCES

-
1. M. Mansuripur, J. Kevin Erwin, Warren Bletscher, A Polychromatic Dynamic Testbed, (Optical Data Storage Center, Quarterly Report: September 15, 1996, University of Arizona)
 2. G. Bouwhuis, J. Braat, A Huijser, J. Pasman, Principles of Optical Disc Systems, (Adam Hilger Ltd, Bristol and Boston, 1985)
 3. Alan B. Marchant, Optical Recording, (Addison Wesley Publishing Company, 1990)
 4. Standard ECMA, ISO/IEC JTC1.23.14517, WG2 N917 - Revised CD Text
 5. Stanley M. Shinnars, Modern Control System Theory and Application, 2nd ed., (Addison Wesley Publishing Company, 1978)
 6. Optical Disk Drive Subassembly, Publication No. GA32-0310-02, 1995.
 7. M. K. Sundareshan , H. S. Tharp, T. M. Ferris, Improved Controllers for Disk Drive Actuators, (Final Report - Phase I, April 15, 1992)
 8. G.F. Franklin, J.D. Powell, and M.L. Workman , Digital Control of Dynamic Systems, 2nd ed., (Addison Wesley Publishing Company, 1990)
 9. Katsuhiko Ogata, Modern control Engineering, 2nd ed., (Prentice Hall, New Jersey, 1990)